Chemical Engineering Journal 522 (2025) 167327

Contents lists available at ScienceDirect

Chemical Engineering Journal

journal homepage: www.elsevier.com/locate/cej

Spatiotemporally adjustable hybrid hydrogels interconnected by 2D MXene for combinatorial therapy of infected diabetic wounds

Mrinmoy Karmakar [a,1], Sungyun Kim [a,b,1], Han-Jun Kim [c,d], Ji Won Huh [a], Da In Jeong [a], Eunseo Park [a], Seongeun Kim [a], Eun-Hye Hong [a], Jin Hyeong [a], Dae-Joon Kim [a], Hye Kyu Choi [b], Junmin Lee [e], Hyun-Jeong Ko [a], Ki-Bum Lee [b], Dae-Duk Kim [f], Hyun-Jong Cho [a,*]

[a] Department of Pharmacy, Kangwon National University, Chuncheon 24341, Republic of Korea
[b] Department of Chemistry and Chemical Biology, Rutgers, The State University of New Jersey, 123 Bevier Road, Piscataway, NJ 08854, USA
[c] College of Pharmacy, Korea University, Sejong 30019, Republic of Korea
[d] Interdisciplinary Major Program in Innovative Pharmaceutical Sciences, Korea University, Sejong 30019, Republic of Korea
[e] Department of Materials Science and Engineering, Pohang University of Science and Technology (POSTECH), Pohang 37673, Republic of Korea
[f] College of Pharmacy and Research Institute of Pharmaceutical Sciences, Seoul National University, Seoul 08826, Republic of Korea

ARTICLE INFO

Keywords:
Diabetic wound healing
Hybrid hydrogel composite
MXene
Peptide
Terpolymer

ABSTRACT

Spatiotemporally adjustable and multifunctional bioresponsive dual-crosslinked hydrogels (MultiBioGel) were developed by integrating two-dimensional (2D) MXene nanosheets into a peptide-annealed terpolymer matrix *via* response surface methodology-optimized fabrication. This 2D nanostructure-entangled hydrogel system harnesses the combinatorial contributions of MXene's reactive oxygen species (ROS)-scavenging and photothermal properties, the mechanical durability and pH-responsive nature of the poly(acrylic acid-*co*-3-acrylamidopropanoic acid-*co*-acrylamide) network, and daptomycin (DPT)'s antimicrobial activity. Our MultiBioGel hydrogel integrates (i) a mechanically robust dual-crosslinked terpolymer matrix, (ii) MXene, which provides redox-mediated ROS/reactive nitrogen species scavenging and photothermal antibacterial activity, and (iii) DPT, a potent gram-positive membrane-disruptive antibiotic. This design enables rapid gelation, injectability, shape adaptability, sustained drug release, and combinatorial antibacterial performances under near-infrared light irradiation—features that are often absent or underdeveloped in traditional natural polymer-based hydrogels. In addition, the hydrogel promotes tissue regeneration through epidermal renewal, angiogenesis, and macrophage polarization. This hybrid hydrogel platform demonstrated potent therapeutic efficacy in both non-infected and bacteria-infected diabetic wound models, offering a promising solution for advanced combinatorial wound healing therapy.

1. Introduction

Chronic diabetic wounds present a significant global health challenge, often resulting in prolonged inflammation, bacterial infection, tissue necrosis, and a high risk of amputation [1–3]. These wounds are difficult to manage due to impaired angiogenesis, elevated oxidative stress, and poor immune responses. In particular, infection caused by antibiotic-resistant bacteria is a major barrier to effective healing, frequently leading to delayed closure and recurrence [4]. As such, there is an urgent clinical need for advanced wound care systems that integrate antimicrobial, antioxidative, and regenerative functionalities.

Hydrogel systems have gained attention for wound healing because of their inherent properties, such as soft structures adaptable to wound area, water storage for moisture-rich healing, porous space for oxygen passage, drug delivery capability, biocompatibility, and extracellular matrix-mimetic feature [5]. Many pH-responsive hydrogels have drawn attention in wound healing as they can deliver therapeutic payloads, such as anti-inflammatory and antibacterial drugs and growth factors [6]. Copolymers of acrylic monomers, such as acrylamide (AAm) and acrylic acid (AA), contribute to biocompatibility and tunable properties, such as hydrophilicity, water retention, pH-responsivity, and antibacterial activity [5]. The crosslinked hydrogel network provides

* Corresponding author.
E-mail address: hjcho@kangwon.ac.kr (H.-J. Cho).
[1] These authors contributed equally to this work.

https://doi.org/10.1016/j.cej.2025.167327
Received 19 May 2025; Received in revised form 5 August 2025; Accepted 15 August 2025
Available online 18 August 2025

mechanical stability and durability, which are essential for designing an effective wound dressing material [5]. However, the crosslinked copolymer of AAm and AA cannot provide a suitable wound dressing formulation for chronic diabetic and infected wounds owing to the absence of therapeutic functions.

To enhance the antibacterial performance, daptomycin (DPT)—a clinically approved lipopeptide antibiotic—is an attractive candidate due to its potent membrane-targeting mechanism against gram-positive bacteria [7,8]. DPT binds to bacterial membranes in a calcium-dependent manner, causing depolarization and cell death [7,8]. However, its activity is limited to gram-positive bacteria, and it does not modulate oxidative stress or tissue inflammation. To overcome these limitations of DPT and provide multifunctional support in the wound microenvironment, MXene (with near-infrared (NIR) light) was introduced as a complementary agent.

MXenes—a novel class of two-dimensional (2D) nanomaterials—display metal-like electrical conductivity, can be readily processed in aqueous solutions, possess robust mechanical strength, are highly biocompatible, and offer efficient photothermal conversion capabilities [9,10]. The photothermal conversion efficiency of MXene exceeds that of conventional photothermal agents like graphene oxide and gold nanoparticles [11]. MXene possesses fair redox-mediated scavenging activities against reactive oxygen species (ROS) (*e.g.,* H_2O_2, $^{\bullet}OH$, and $O_2^{\bullet-}$) and reactive nitrogen species (RNS) (*e.g.,* $NO^{\bullet}$ and $NO_2^{\bullet}$). MXenes have excellent antibacterial properties against both gram-negative and gram-positive bacteria and electrical conductivity [12,13]. Therefore, MXene-based hydrogels are gaining attention for developing wound healing materials. Various natural polymers, such as hyaluronic acid and sodium alginate, have been combined with MXene and therapeutic additives to develop hydrogel systems for wound healing applications [12–16]. Despite the promising therapeutic potential of MXene-integrated gels, existing MXene/polymer systems have limited mechanical durability and suboptimal antibacterial performance in diabetic wound environments. Macroporous hydrogels incorporating MXene lacked long-term mechanical stability under moist conditions, leading to structural failure and reduced therapeutic efficiency [15]. Similarly, while MXene-based gels can impart antibacterial activity, they often require external agents or modifications to enhance pharmacological effects [16]. These limitations necessitate a more robust design strategy integrating a mechanically stable polymeric framework with antibacterial agents. In this study, we addressed these limitations by developing a terpolymer hydrogel, with superior mechanical performance, photothermal responsiveness, and antibacterial combination, using MXene and DPT. To the best of our knowledge, studies on the development of antibacterial peptide-loaded MXene-grafted-robust terpolymer-based hydrogels, with rapid gelation in open air, injectability, pH-responsivity, biocompatibility, shape adaptability, bioadhesiveness, mechanical sustainability, conductivity, photothermal activity, sustained drug release, ROS/RNS scavenging ability, antibacterial property, and wound healing capability, have not yet been reported.

This study presents a one-pot aqueous-phase synthesis method for a multifunctional bioresponsive dual-crosslinked hydrogel (MultiBioGel)—DPT-internalized-MXene-*g*-poly[AA-*co*-3-acrylamidopropanoic acid (AAMPPA)-*co*-AAm] (DMH). It was prepared by mixing initiator solution with hydrogel precursor at room temperature in open air. For the first time, *in situ* N—H activated conversion of $–CONH_2$ in AAm to –CONH– with MXene was achieved in a short gelation time (~90 s), without external transition metal-based catalysts. *Ex situ* AA and AAm introduce softness and shape adaptability based on wound dimension, swelling ability, hydrophilic functionality, and pH-responsivity for drug entrapment and programmed delivery; *in situ* generated AAMPPA elevates mechanical robustness enabling DMH to maintain integrated structure for more than 15 days in biological fluids; MXene imparts ROS scavenging, photothermal activity, and mild antibacterial potential; and DPT induces strong antibacterial effects with tissue regeneration and re-epithelialization. DMH (MultiBioGel), obtained by combining the properties of MXene and DPT, is expected to exhibit better wound characteristics than those of counter hydrogels, such as poly[AA-*co*-3-AAMPPA-*co*-AAm] (BH), MXene-*g*-BH (MH), and DPT-loaded-BH (DH). This hybrid hydrogel system offers superior and rapid healing of full-thickness diabetic and infected wound based on optimized physicochemical and mechanical features.

2. Materials and methods

2.1. Materials

Dimethyl sulfoxide-d_6 (DMSO-d_6), H_2O_2 solution (30 % *w*/w in H_2O), $TiOSO_4$ solution (1.9–2.1 %), 3,3′,5,5′-tetramethylbenzidine dihydrochloride hydrate (TMB DH), nitroblue tetrazolium (NBT), 2,7-dichlorodihydrofluorescein diacetate (DCFH-DA), sodium chloride (NaCl), calcium chloride dihydrate ($CaCl_2{\cdot}2H_2O$), and glutaraldehyde solution (25 % in H_2O) were obtained from Sigma-Aldrich (Saint Louis, MO, USA). AA, AAm, DPT, methylene blue (MB, hydrate form), *N*,*N*′-methylene bisacrylamide (MBAm), potassium persulfate ($K_2S_2O_8$), sodium bisulfite ($NaHSO_3$), 5,5-dimethyl-1-pyrroline *N*-oxide (DMPO), riboflavin, and D,L-methionine were purchased from Tokyo Chemical Industry Co. Ltd. (Tokyo, Japan). Dulbecco's modified Eagle's medium (DMEM), Dulbecco's phosphate buffered saline (DPBS), and fetal bovine serum (FBS) were obtained from Welgene Inc. (Gyeongsan, Republic of Korea). Penicillin–streptomycin was acquired from Gibco Life Technologies, Inc. (Grand Island, NY, USA).

2.2. Synthesis of MXene and its analysis

MXenes were synthesized by etching of the MAX phase with a slightly modified method [10]. In a brief, dried MAX powder (0.5 g) was mixed firmly with NH_4F (2.6 g) in an Erlenmeyer flask, followed by heating the flask to 60 °C in a water bath. After homogenization at 60 °C, concentrated HCl (15 mL) was added dropwise to the mixture to initiate the etching of Al-layers of MAX. The reaction was vigorously processed in the beginning phase and then settled down after 30 min. This etching process continued for 6 h, and then, a solid black-colored MXene was isolated by centrifugation, washed thoroughly by distilled water (DW) until it became acid-free, and dried in a hot-air oven.

The conversion of MAX into MXene was confirmed by an X-ray diffractometer (XRD, D8 Discover, Bruker Corp., Billerica, MA, USA). Spectra were recorded within 5–80° of 2θ using the CuK_α source of 5.4 kW. The d-spacing values were calculated using Bragg's Law (Eq. (1A)). The average particle size from the XRD peak was calculated using the Scherrer equation (Eq. (1B)).

$$n\lambda = 2dsin\theta \tag{1A}$$

$$\tau = \frac{k\lambda}{\beta cos\theta} \tag{1B}$$

Here, n, λ, τ, k, and β represent the order of diffraction (an integer), wavelength of X-ray light, particle size, shape factor, and full-width half maximum of XRD peak, respectively.

The particle size and zeta potential of MXene were analyzed using a Zetasizer NanoZS90 (Malvern Panalytical, Malvern, UK).

Internal shapes of MAX, MXene, and MH were observed by field emission-scanning electron microscopy (FE-SEM, JSM-7900F, JEOL Ltd., Akishima, Japan). Before their analysis, each specimen was coated with Pt.

Layered structure and interplanar distance of the as-synthesized MXene was observed by high-resolution transmission electron microscope (HR-TEM, Tecnai G^2 F30, FEI company, Hillsboro, OR, USA) at the operating voltage of 300 kV.

2.3. Fabrication of hydrogels and their structural evaluation

MH was synthesized *via* free-radical solution polymerization using an optimized synthesis composition at an optimal temperature. Optimization was performed by measuring the equilibrium swelling ratio (ESR) of the hydrogels synthesized according to the response surface methodology (RSM) design, considering the combinational effects of multiple factors on ESR while conducting minimum number of experiments [17]. Since six parameters, such as molar ratio of AA/AAm (*A*, –), temperature (*B*, °C), amounts of MBAm (*C*, wt%), initiators (*D*, wt%), monomers (*E*, wt%), and MXene (*F*, mg/mL), can modulate structural robustness of MH, all of these factors should be varied in RSM approach. To reduce the volume of experiments, a two-stage RSM design constituting stage-I (resolution-IV) and stage-II (face-centered central composite design (FCCD)), was employed. In stage-I, optimization of these six parameters was carried out by using 2-level factorial design and reduced 3FI (R3FI) model and unary/binary interactions among parameters. The three most influential parameters identified from stage-I were optimized in stage-II by using the FCCD design (quadratic model containing 2^p, 2p, and p_c amounts of factorial, axial, and central runs, respectively [p = number of parameters]).

Based on optimum conditions for DMH, AA (4.55 g) was neutralized to pH 5.5 by saturated aqueous NaOH, followed by adding AAm (0.45 g) and MBAm (0.5 g). The volume was made up to 15 mL with DW and homogenized for 60 min. Monomer mixture (0.8 mL) was withdrawn and dried MXene (2 mg) was added. This was treated by an ultrasonic processor for 10 min to achieve homogeneous dispersion of MXene with reactants. DPT (2 mg) was added and homogenized for 2 h. Polymerization was initiated by adding initiator solution ($K_2S_2O_8$ + $NaHSO_3$ (0.08 g + 0.08 g) in DW (0.2 mL)). Rapid sol-to-gel transformation occurred at room temperature without an inert environment. DMH was collected and washed with a water/methanol mixture (1:3 (*v*/v)). Lyophilized products were acquired for further use. BH, DH, and MH were synthesized using the same protocol, except for adding MXene and/or DPT.

Structural elucidation of DMH was carried out using a proton nuclear magnetic resonance (^{1}H NMR) spectrometer (Avance Neo 600, Bruker Ltd., Billerica, MA, USA) after dispersing in DMSO-d_6.

The thermal properties of BH and DMH were determined by thermogravimetry (TG) analysis (TGA; SDT Q600, TA instruments, New Castle, DE, USA). Spectra were recorded within 35–600 °C in a nitrogen atmosphere at a heating rate of 10 °C/min.

Dried BH, MH, DPT, and DMH were prepared for Fourier-transform infrared (FT-IR) analyses. Wavenumber-dependent transmittance values were obtained by FT-IR spectrometer (PerkinElmer Inc., Waltham, MA, USA) with attenuated total reflectance (ATR) mode. Transmittance profiles were obtained within 400–4000 cm^{-1}.

For measuring pH at the point of zero charge (pH_{PZC}) of BH, a definite amount (0.2 g) of solid BH was added to each buffer solution (25 mL) of different initial pH (pH_i), ranging from ~1 to 10, with constant stirring at 200 rpm. After 72 h stirring, the final pH, *i.e.*, pH_f, of each solution was measured. Then $\Delta pH = pH_f - pH_i$ was plotted against pH_i. The pH_{PZC} of BH could be obtained from pH_i at the zero ΔpH.

Binding patterns of MXene and DPT with BH were investigated by X-ray photoelectron spectroscopy (XPS) analysis (K-Alpha$^+$, Thermo Fisher Scientific, Waltham, MA, USA). MXene, BH, MH, and DMH samples (dried form) were prepared, and elemental analyses were conducted.

2.4. Rheological and mechanical assessments of hydrogel systems

The morphological properties of the lyophilized BH and DMH were determined by FE-SEM. Before analysis, each lyophilized specimen was coated with Pt. The pore size was calculated using ImageJ software [18].

Gelation behavior of each specimen was investigated by an inversion test. BH, DH, MH, and DMH specimens were prepared and their photographs in the inverse positions were acquired. The crosslink density (CD) values of the hydrogels were measured using Eq. (2) [19].

$$CD = \frac{\ln(1 - V_p) + V_p + \chi V_p^2}{V_w D_p \left(V_r^{1/3} - V_p^2\right)} \tag{2}$$

Here, V_p, D_p, χ, V_r, V_w, and m_w represent the equilibrium hydrogel volume fraction in water, density of hydrogel, water–hydrogel interaction parameter, molar volume of water, volume fraction of water in swelled hydrogels, and molar weight of water, respectively. However, V_p and χ could be computed using Eq. (2A) and Eq. (2B).

$$V_p = \frac{1/D_p}{(m_w/0.99) + (1/D_p)} \tag{2A}$$

$$\chi = \frac{V_p}{3} + 0.5 \tag{2B}$$

Each specimen (50 mg) of dried BH, MH, DH, and DMH (W_i) was incubated in 20 mL of phosphate-buffered saline (PBS, pH 7.4 and 8.5). Each specimen was withdrawn at 0.5, 1, 2, 4, 6, 12, 24, 48, and 72 h and wrapped with tissue paper to remove the adhered liquid on the outer surface of the hydrogels. Then, the hydrogels were unwrapped, weighed (W_f), and placed into the tubes again. The swelling ratio (SR, %) was determined using Eq. (3).

$$\text{SR}\ (\%) = \frac{W_f - W_i}{W_i} \times 100 \tag{3}$$

For calculating the ESR (%), each hydrogel was incubated in DW till the final weight (W_f) became constant, which indicated the achievement of equilibrium (W_e). ESR was calculated using Eq. (3A).

$$ESR\ (\%) = \frac{W_e - W_i}{W_i} \times 100 \tag{3A}$$

The rheological features of BH, DH, MH, and DMH samples were measured with rheometer (MCR 302, Anton Paar GmbH, Graz, Austria). The variation of storage modulus (G′) and loss modulus (G″) with strain and frequency sweep was measured by the varying strain within 1–402 % and frequency within 1–100 rad/s by keeping frequency and strain at 10 rad/s and 10 %, respectively. All the experiments were carried out using 25 mm parallel plate and 1 mm gap height at 37 °C. Shear rate-dependent viscosity profiles of BH and DMH samples were obtained at 0.01–100 s^{-1} shear rate range.

The mechanical stability of hydrogels was studied by measuring tensile stress and compressibility stress using a universal testing machine (QM100S, Qmesys, Uiwang, Republic of Korea). BH, DH, MH, and DMH of unified shapes were incubated in DW and PBS for 30 min and 72 h to obtain swelling and equilibrium swelling, respectively, before measuring tensile stress and compressibility stress of DMH in both conditions at 10 kgf load capacity. For tensile stress measurement, samples of consistent dimensions (width and thickness of 5 and 3 mm, respectively) were prepared using a testing gauge length of 5 mm. Young's modulus was estimated from the slope of the initial linear portion (*i.e.*, yield point (YP)) of tensile stress *vs.* strain curve and ultimate strength was obtained from the fracture point (FP). Toughness was calculated by measuring the area under the tensile stress *vs.* strain curve. For compressibility stress, samples were prepared in cylindrical shapes of consistent dimensions (height and diameter of 10 and 15 mm, respectively).

Conductivity measurements of BH and DMH were measured by electrical impedance spectroscopy (EIS) through a three-electrode method using an electrochemical workstation (CHI660D, CH Instruments, Inc., Austin, TX, USA). Before experiments, hydrogel specimens were incubated in PBS (pH 7.4) for 30 min, then sandwiched between two parallel indium tin oxide (ITO)-coated glass plates. The three-electrode system was assembled with working, auxiliary

(platinum wire), and reference (Ag/AgCl) electrodes. The cyclic voltammetry (CV) experiment was conducted at 50 mV/s using the same instrument. The working potential of each hydrogel was determined from the potential window of the CV plot. For measuring transepithelial potential (TEP), the working potential in each unit dimension of hydrogel was calculated by dividing the working potential by the hydrogel dimension.

Shape adaptiveness of DMH was tested by spreading it onto the finger and bending. For measuring stretchability, hydrogels of specified length (L_i, cm) were pulled until the breaking point (L_f, cm). The stretchability (%) was estimated using Eq. (4).

$$Stretchability\ (\%) = \frac{L_f - L_i}{L_i} \times 100 \quad (4)$$

Similarly, DMH was twisted and rolled up to ensure its structural flexibility. Adhesiveness of DMH to the plastic dish was also assessed.

Freshly prepared DMH was immersed in water, followed by bending, twisting, rolling, and adhesion with glass, and images were captured through digital camera.

The adhesive strength of DMH to porcine skin tissue was evaluated by lap shear experiments using a universal testing machine. DMH (1 cm × 1 cm) and porcine skin (1 cm × 1 cm) were fixed onto each glass slide using commercial glue. The control group was prepared with two porcine skin tissues attached to each glass slide. The slides were connected *via* porcine skin and DMH, followed by measuring tensile stress at 37 °C to calculate DMH's bioadhesive strength.

For measuring underwater adhesion force, DMH (1 cm × 1 cm) was fixed with one glass slide by commercial glue. Then the entire assembly was immersed into DW, and DMH was covered by another porcine skin prefixed with another glass slide. After that, this assembly was carefully lifted from DW, attached with the tensile stress measuring instrument to calculate the adhesive stress.

Bioadhesion mechanisms of DMH to porcine skin were explored by FT-IR spectroscopic analysis with ATR technique within 400–4000 cm^{-1}. DMH was incubated in DW for 30 min and cut into (8 mm × 3 mm) dimensions. Skin tissue was cut to 10 mm × 4 mm, and DMH was placed on this tissue using forceps to prepare tissue–DMH samples.

To evaluate *ex vivo* adhesion of DMH with different tissues, vital organs (heart, kidney, spleen, lung, and liver) of C57BL/6N mice (male, body weight: ~20 g; Koatech, Pyeongtaek, Republic of Korea) were collected and placed on DMH (0.2 mL; incubated in DW for 1 h at 37 °C) adhered to a glass slide. All animal studies were approved by the Animal Care and Use Committee of Kangwon National University and conducted according to the National Institutes of Health (NIH) Guide for the Care and Use of Laboratory Animals (NIH Publications No. 8023, revised 1978). After 5 min, organ adhesion with DMH was photographed.

The *in vivo* spreading capability of DMH was studied by covering the wound site of the mouse with DMH (0.3 mL). Following an application for 24 h, images were taken, and the weight of hydrogels recovered from the mouse wound was measured (W_f) together with the initial weight of applied DMH (W_i). The spreadability (%) was calculated using the following Eq. (5).

$$\text{Spreadability}\ (\%) = \frac{W_f}{W_i} \times 100 \quad (5)$$

The *in vitro* hemostatic capability of BH and DMH was confirmed by measuring blood clotting index (BCI) using the methodology described elsewhere [20]. The lyophilized samples and cotton gauze (positive control) were cut into cylindrical shapes of consistent diameter. Blood specimens were obtained from Sprague Dawley rat (male, body weight: ~250 g, Koatech). Recalcified fresh blood solution (0.05 mL containing 10 mM $CaCl_2$) was added to samples and control groups, pre-warmed at 37 °C. After incubating at 37 °C for 150 s, DW (10 mL) was added to release unbound blood without disturbing the clot. Images were taken by digital camera and absorbance values of the supernatant were recorded at 540 nm using a microplate reader (SpectraMax i3, Molecular Devices, Sunnyvale, CA, USA). The absorbance of recalcified blood (0.05 mL) diluted in DW (10 mL) served as the reference (negative control). BCI was calculated using the following Eq. (6).

$$\text{BCI}\ (\%) = \frac{I_s - I_0}{I_r - I_0} \times 100 \quad (6)$$

Here, I_s, I_r, and I_0 represent the absorbance *v*alues of the samples, reference (*i.e.*, negative control), and DW, respectively.

The blood clotting time was calculated by using a slightly modified protocol [21]. Fresh rat blood was transferred to sodium citrate-containing vacutainer (BD Vacutainer, Franklin Lakes, NJ, USA). To initiate coagulation, 0.05 M $CaCl_2$ solution was added to the citrated blood at a 10:1 ratio, followed by vortex-mixing. After that the recalcified blood (0.1 mL) was added to each well of a 96 well-plate containing 0.05 mL of BH and DMH. For the control group, the recalcified blood (0.1 mL) was added to the empty wells. At predetermined time intervals, each well was gently washed with 0.9 % (w/v) NaCl solution until the washing solution became clear, indicating the removal of soluble components from unclotted blood. The clotting time was determined as the time required to form a stable clot that remained after washing.

For studying the *in vivo* hemostatic property of DMH, the liver of Sprague Dawley rat (male, body weight: ~250 g, Koatech) was excised by an 8-mm-diameter punch and scissors, and the blood ejected from the liver was soaked on a dry filter paper. DMH (0.2 mL) was added to observe the blood-clotting behavior following punching, whereas, for control group, only PBS was applied after punching. The amount of blood collected on the tissue was measured to obtain blood loss value (%).

The *in vitro* hemolysis test was conducted by the reported method [22]. Fresh rat blood (1 mL) was suspended in PBS (10 mL) with heparin sodium (0.05 mL), followed by centrifugation at 1000 rpm for 15 min to isolate red blood cells (RBCs) from plasma. The separated RBCs were washed thrice with PBS until the supernatant became colorless. A definite volume (0.05 mL) of BH and DMH was put into the conical tube with PBS (0.2 mL), followed by adding diluted blood (0.2 mL) into each tube. Blood was added with 0.1 % Triton X-100 (0.2 mL) and PBS (0.2 mL) for positive and negative controls, respectively. After incubating for 1 h at 37 °C, specimens were centrifuged at 1000 rpm for 15 min, supernatant was withdrawn, and absorbance values were measured at 540 nm using a microplate reader. The hemolysis portion was calculated using the following Eq. (7) [22].

$$\text{Hemolysis}\ (\%) = \frac{OD_t - OD_n}{OD_p - OD_n} \times 100 \quad (7)$$

Here, OD_t, OD_n, and OD_p represent the absorbance values of the test samples, negative control, and positive control, respectively.

2.5. In vitro antibacterial and wound healing tests

The antimicrobial studies were conducted against gram-positive (*S. aureus*; Korean Collection for Type Cultures, Jeongeup, Republic of Korea) and gram-negative (*E. coli*; Korean Collection for Type Cultures) bacteria *via* disk-diffusion method. Bacterial suspension (0.1 mL, 1.0 × 10^7 CFU/mL) was cultured on Mueller Hinton agar plates (90 mm diameter). Hydrogel samples (BH, DH, MH, and DMH) were placed in those agar plates and incubated at 37 °C. MH and DMH samples were irradiated by NIR light (808 nm and 1 W/cm^2) for 3 min. After 24 h incubation at 37 °C, diameter of inhibition zone (DIZ) was measured. Next, to the bacterial suspension (0.1 mL, 1.0 × 10^7 CFU/mL), definite volume (0.1 mL) of DPT (2 mg/mL) and released solutions of hydrogel specimens (after adding 0.3 mL specimens to 0.5 mL DW) were added and incubated at 37 °C for 3 h. Then definite volumes (20 μL) of each bacterial suspensions were fixed on carbon tapes by using 2.5 vol% of

glutaraldehyde solution, followed by capturing their FE-SEM (SU8600, Hitachi, Tokyo, Japan) images. Also, definite volumes (0.1 mL) of these mixtures were spread evenly on the agar plates. After 24 h incubation at 37 °C, digital images of the plates were captured to compare the bacterial colony growth in-presence of hydrogel samples with those of controls.

Photothermal properties of hydrogels were studied using NIR light (1 W/cm^2) at 808 nm. For evaluating the *in vitro* photothermal effect, each specimen (1 mL) of DW, BH, DH, MH, and DMH was put into plastic cuvettes and exposed to NIR light irradiation for 3 min. Temperature change was measured using a thermal camera (FLIR E8, FLIR Systems, Inc., Wilsonville, OR, USA) and dual thermometer (8856 AZ EB, AZ Instrument Corp., Taichung, Taiwan). Photothermal conversion efficiency was measured by repeating cycles of NIR light irradiation for 5 min and cooling for 5 min.

Released profiles of DPT from DMH were investigated at pH 6.2, 7.4, and 8.5. DPT-incorporated hydrogel (corresponding to 0.75 mg/mL of DPT, 0.2 mL) was added to release media (2 mL) and incubated at 37 °C in a water bath with 50 rpm agitation. Release medium (0.2 mL) was obtained at 1, 2, 4, 12, 24, 48, 120, 240, 360, 480, and 600 h. An equivalent volume of fresh media was added at each sampling time. DPT concentration was analyzed by high-performance liquid chromatography (HPLC) system (1260 Infinity II, Agilent Technologies, Santa Clara, CA, USA) with a reverse phase C18 column (Kinetex, 250 mm × 4.6 mm, 5 μm, 100 Å; Phenomenex, Torrance, CA, USA). Mobile phase comprised 1 M phosphate buffer (pH 3.1) and acetonitrile (6:4, v/v). Analysis was performed under isocratic conditions at 1 mL/min flow rate. Each specimen (10 μL) was injected, and chromatograms were acquired at 262 nm.

The drug release mechanism was evaluated by using mathematical modelling, reported elsewhere [23]. Briefly, fraction of drug release (M_t/M_∞) can be related to time of release (t) by the equation:

$$\frac{M_t}{M_\infty} = kt^n \tag{8}$$

Here, k and n represent geometry constant and drug release exponent, respectively. The value of n can be obtained from the slope of the straight line obtained by plotting the release data against release time in logarithmic scale.

H_2O_2-scavenging capability of hydrogels was tested with $TiOSO_4$. In following ROS and RNS scavenging assays, ascorbic acid (Asc) was used as an antioxidant agent. Aliquots (0.3 mL) of Asc solution (0.1 mg/mL), MXene dispersion (2 mg/mL in DW), BH, DH, MH, and DMH were inserted into a dialysis membrane (molecular weight cut-off (MWCO): 12–14 kDa) and incubated at 37 °C in 1 mM H_2O_2 solution (5 mL). Aliquots (0.1 mL) were withdrawn at 6, 24, 48, and 72 h, followed by adding 30 mM $TiOSO_4$ solution (0.1 mL). Absorbance was detected at 405 nm with a microplate reader.

$^\bullet$OH scavenging property was estimated by TMB assay. Asc solution (0.1 mg/mL), MXene dispersion (2 mg/mL in DW), BH, DH, MH, and DMH (0.3 mL) were incubated at 37 °C in PBS (5 mL). Aliquots (0.2 mL) were collected at 6, 24, 48, and 72 h. Then, 0.03 % H_2O_2 (0.2 mL), 30 mM $FeSO_4$ (0.2 mL), and 0.5 M acetic acid buffer (pH 4.5) were mixed with samples, followed by 1 mM TMB (in DMSO; 0.4 mL). Mixtures were incubated for 10 min and centrifuged at 13,200 rpm for 5 min, and absorbance values were measured at 652 nm. The scavenging efficacy (%) of $OH^\bullet$ was estimated by the following Eq. (9) [24]:

$$\text{Scavenging (\%)} = \left[1 - \left(\frac{A_1 - A_2}{A_0}\right)\right] \times 100 \tag{9}$$

Here, A_0, A_1, and A_2 represent absorbance values of control (DW instead of sample), samples, and background (DW instead of H_2O_2), respectively.

Additionally, $^\bullet$OH scavenging efficiency of hydrogels was further evaluated by using an MB assay. Determined volume (0.3 mL) of Asc solution (0.1 mg/mL), MXene dispersion (2 mg/mL in DW), BH, DH, MH, and DMH was incubated at 37 °C in PBS (5 mL). Determined volume (0.2 mL) of specimens (from released samples) was added into conical tubes, followed by the addition of 0.03 % H_2O_2 in DW (2 mL). The mixture was incubated for 30 min, followed by the addition of MB solution (20 μg/mL, 2 mL). All the samples were incubated at 37 °C for 30 min, followed by the measurement of the absorbance values at 650 nm by a microplate reader.

The $O_2^{\bullet-}$ scavenging efficiency was measured by NBT assay. For this, definite volume (0.3 mL) of Asc solution (0.1 mg/mL), MXene dispersion (2 mg/mL in DW), BH, DH, MH, and DMH was incubated at 37 °C in PBS (5 mL). From these released samples, the determined volume (0.2 mL) of all the specimens was added into conical tubes. After that, these samples were added to a mixture (3 mL) of 20 μM riboflavin, 12.5 mM D, L-methionine, and 75 μM NBT. Mixtures were incubated at 37 °C for 10 min, and absorbance values were measured at 560 nm using a microplate reader. The scavenging (%) of $O_2^{\bullet-}$ was calculated using the following Eq. (10) [25].

$$\text{Scavenging (\%)} = \left(\frac{A_0 - A_n}{A_p - A_n}\right) \times 100 \tag{10}$$

Here, A_0, A_p, and A_n represent absorbance values of samples, positive control (mixture of riboflavin, methionine, and NBT in DW under ultraviolet radiation for 15 min), and negative control (mixture of riboflavin, methionine, and NBT in DW), respectively.

For 2,2′-azino-bis(3-ethylbenzothiazoline-6-sulfonic acid) (ABTS) and 1,1-diphenyl-2-picrylhydrazil (DPPH) assays, 0.3 mL of Asc solution (0.1 mg/mL), MXene dispersion (2 mg/mL in DW), BH, DH, MH, and DMH was incubated at 37 °C in release media. At 6, 24, 48, and 72 h, 0.2 mL was withdrawn from each sample and an equal amount of release media was added to maintain volume. Withdrawn solutions were divided into two 0.1 mL parts for ABTS and DPPH assays. Then 7.4 mM ABTS solution was mixed with 2.6 mM $K_2S_2O_8$ at room temperature and stored in the dark for 24 h to generate radicals. This solution was diluted 25 times by PBS (pH 7.4) to obtain an absorbance of ~0.7 at 732 nm, followed by adding sample solutions (0.1 mL) to fresh ABTS-radical solutions (0.1 mL). Samples reacted for 30 min in the dark before measuring absorbance at 732 nm using a microplate reader. For DPPH, sample solutions (0.1 mL) were added to fresh 0.1 mM DPPH (0.1 mL in ethanol) solutions, placed in the dark for 30 min, and absorbance was measured at 517 nm.

Electron paramagnetic resonance (EPR) analysis verified $^\bullet$OH scavenging. H_2O_2 (10 mM, 0.2 mL) was mixed with $FeSO_4$ (30 mM) in 0.5 M acetic acid buffer (0.2 mL) to generate $^\bullet$OH. This solution (0.2 mL) was added to tubes containing MXene dispersion and DMH (0.6 mg/mL MXene). DMPO solution (100 mM, 0.5 mL) was mixed with the mixture. After 30 min at 37 °C, specimens were analyzed by EPR spectrometer (JES-X320, JEOL Ltd.).

The antioxidant mechanism of MXene was evaluated by XPS analysis. H_2O_2 (10 mM, 0.2 mL) was mixed with $FeSO_4$ (30 mM) in 0.5 M acetic acid buffer (0.2 mL) to generate $^\bullet$OH. This solution (0.2 mL) was added to tube containing MXene dispersion (0.6 mg/mL MXene). After 30 min incubation at 37 °C, the resultant dispersion was centrifuged, supernatant was discarded, black residues of the oxidized MXene particles were washed with DW, and dried at 50 °C for 72 h. Then XPS analysis of these oxidized MXene particles were recorded.

Cellular ROS scavenging properties were studied in NIH3T3 cells. NIH3T3 cells (Korean Cell Line Bank, Seoul, Republic of Korea) were cultured with DMEM including 10 % (v/v) FBS and 1 % (v/v) penicillin–streptomycin. Cells were seeded in 12-well plates (1×10^5 cells/well) and incubated for 24 h. H_2O_2 solution (10 mM, 0.1 mL) was added and incubated for 6 h. Hydrogel samples (0.05 mL) were loaded onto polymer membrane insert system (12-well plate, SPLInsert Hanging tubes, SPL Life Sciences, Pocheon, Republic of Korea) and incubated with cells for 72 h. At 72 h, media of each specimen was removed, cells

were washed twice with PBS (pH 7.4), and stained with DCFH-DA (10 μM) for 20 min at 37 °C. Cells were resuspended in DPBS and analyzed by fluorescence microscopy.

To examine whether hydrogel samples have stimulatory effects on cell migration, the scratch wound healing assay was performed with NIH3T3 cells. The cells were seeded in a 12-well plate (at 1×10^5 cells per well) and incubated at 37 °C for 24 h. Each well was scratched by a pipette tip and images of wound areas were taken immediately ($A_{t=0}$). Subsequently, an aliquot (0.05 mL) of each specimen (*i.e.,* BH, DH, MH, and DMH) was loaded onto the inner part of the polymer membrane insert system, assembled with well plate which cells were grown on the bottom, and incubated at 37 °C for 72 h. Photographs of wound areas were recorded at 24, 48, and 72 h ($A_{t=t}$). The filling of the scratch area (*i.e.*, WC) was measured using ImageJ software [18]. The percentage gap-filling (WC, %) can be calculated by the Eq. (11) [26].

$$\mathrm{WC}\ (\%) = \frac{\mathrm{A_{t=0}} - \mathrm{A_{t=t}}}{\mathrm{A_{t=0}}} \times 100 \tag{11}$$

The cytotoxicity of BH, DH, MH, and DMH was examined using live/dead assay on NIH3T3 cells. Cells (1.0×10^5 cells per well) were seeded into 12-well plate and cultured for 24 h. Cells were scratched by pipette tip, followed by the addition of the determined volume (0.05 mL) of hydrogels into the polymer membrane insert system. Cells were incubated for 72 h at 37 °C, sample-loaded insert was removed, cells were washed by DPBS (pH 7.4) thrice, and reagent dyes of live/dead viability/cytotoxicity kit (Thermo Fisher Scientific) (1 mL) were treated to cells following manufacturer's protocols. After 30 min incubation, dyes were removed, cells were washed by DPBS, and fluorescence signals of calcein AM (green channel, live cells) and EthD-1 (red channel, dead cells) were captured using an inverted microscope.

2.6. In vivo wound healing studies in non-infected diabetic mouse models

Streptozotocin (40 mg/kg) in citrate buffer (pH 4.5) was injected into C57BL/6N mice (male, ~20 g, Koatech) for 5 days to induce diabetes mellitus (blood glucose >16.1 mmol/L). These mice were epilated on their backs, and full-thickness wounds were created by skin biopsy punches (8 mm) under inhalation anesthesia. For assessing the wound healing potential of hydrogels, mice were assigned to groups: control (Tegaderm), DPT, MH, MH + NIR, DMH, and DMH + NIR. Each specimen (0.1 mL) was applied to the wound site (0.3 mg/mL of DPT). On days 0, 2, 4, 7, and 9, NIR light (808 nm and 1 W/cm^2) was applied to MH + NIR and DMH + NIR groups for 3 min and wound photos were captured. After the experiment, skin wound tissues from sacrificed mice were collected for histological analysis *via* hematoxylin and eosin (H&E), Masson's trichrome (MT), and immunofluorescence (IF), using CD68 antibody (Ab) (CD68 (E3O7V) rabbit mAb, Cell Signaling Technology, Danvers, MA, USA) and CD206 Ab (CD206/MRC1 (E6T5J) XP rabbit mAb, Cell Signaling Technology), staining. Wound length, epidermal thickness, and CD206/CD68 ratios were measured. *In vivo* safety was investigated through H&E staining of vital organs and blood biochemistry. Heart, kidney, liver, lung, and spleen were obtained and stained with H&E reagent. Blood samples were collected and serum levels of aspartate aminotransferase (AST), alanine aminotransferase (ALT), albumin (ALB), and blood urea nitrogen (BUN) were measured using AU480 chemistry analyzer (Beckman Coulter, Brea, CA, USA).

2.7. Bacteria-infected diabetic wound healing, antibacterial, and toxicity tests

Bacteria-infected diabetic wound model was established to evaluate wound healing and the antimicrobial effects of hydrogels. The induction of diabetic mellitus and wound formation followed the protocol explained previously. Wounds were treated with *S. aureus* suspension (1.0×10^7 CFU/mL, 10 μL) to construct an infected model. After 24 h post-infection, the number of bacterial colonies increased to 10^6 CFU from 10^5 CFU, confirming successful bacterial-infection model establishment. Each specimen (0.1 mL) of DPT, MH, and DMH groups was applied to the wound. Tegaderm was used for the control group. On days 0, 2, 4, 6, 8, and 10, NIR light (808 nm and 1 W/cm^2) was applied to MH + NIR and DMH + NIR groups for 3 min and wound photos were taken.

To assess *in vivo* antibacterial efficacy, swabs from incisional wounds were collected on the final day. Swabs were diluted 10 times using normal saline for quantitative analysis. Each diluted specimen (0.6 mL) was spread onto agar plates (1.5 % agar powder, Sigma-Aldrich) and incubated at 37 °C for 24 h. Photographs were taken and bacterial colony numbers were counted.

At the end of the experiment, skin wound tissues were collected for H&E, MT, and IF staining (*i.e.,* vascular endothelial growth factor (VEGF), CD31, CD68, and CD206). IF staining used VEGF Ab (S04—6D7, Novus Biologicals, Centennial, CO, USA) and CD31 Ab (D8V9E, Cell Signaling Technology) following standard protocols. Relative VEGF and CD31 levels (%) were evaluated by measuring green fluorescence intensity. The skin tissue area in each image represented 100 %. CD206/CD68 ratios were calculated by measuring fluorescence intensity.

Hydrogel safety was assessed through blood biochemistry. Blood samples were collected, and serum levels of AST, ALT, ALB, and BUN were measured using a chemistry analyzer.

2.8. Data analysis

Statistical analysis was carried out using the analysis of variance (ANOVA) method with *post hoc* tests. Each experiment was repeated at least three times. Herein, the data are shown as mean ± standard deviation (SD).

3. Results and discussion

3.1. Therapeutic system concept

Exfoliation of MXene was achieved through a greener method by avoiding direct use of HF (Fig. S1). For the first time, a strong and flexible double-layered DPT-loaded and MXene-grafted-terpolymer hydrogel (DMH) was prepared by *in situ* incorporation of a new monomer with MXene *via* aqueous-phase synthesis in open air, without N_2 (Fig. 1). The MXene (hydrophilic)-to-polymer (hydrophobic) ratio was optimized by RSM. The hydrogel mixture can be injected on wound sites for shape adaptation, with gelation occurring within 90 s. This rapid gelation results from variegated covalent (C–C/N–C coupled), ionic, coordinate, and hydrogen bonds. Consequently, DMH demonstrates shear-thinning behavior, enhanced viscoelasticity and bioadhesiveness, hyperthermic and electrically conductive properties, ROS scavenging activity, rapid hemostatic action, pro-angiogenic potential, antibacterial effects, and macrophage polarization modulation (Fig. 1).

3.2. Structural characterizations of MXene

The XRD data of Ti_3AlC_2 (Fig. S2) shows that the peaks at $2\theta = 9.58$, 19.16, 34.08, 36.80, 38.82, 41.82, 48.44, and 56.42° correspond to (002), (004), (101), (103), (104), (105), (107), and (109) Miller indices, respectively. After etching, the obsolescence of the sharp peak at $2\theta = 38.82°$ indicated Al-planes removal. The peak for (002) plane at $2\theta = 9.58°$ shifted to 6.86° and d-spacing increased from 9.23 Å to 12.88 Å (Eq. (1A)), confirming etching-aided exfoliation of Ti_3AlC_2 [27]. In the case of the MXene, the peaks at $2\theta = 18.20$, 27.30, and 61.20° corresponded to the Ti_3C_2 phase [10], whereas those at $2\theta = 35.28$, 42.62, and 59.18° indicated the presence of TiC phases. According to calculations performed using the Scherrer equation (Eq. (1B)), the average particle sizes of MAX and MXene were 66.3 and 31.0 nm, respectively, which confirmed the nanostructure dimensions of the MXene.

The particle properties of the MXene were evaluated (Fig. S3).

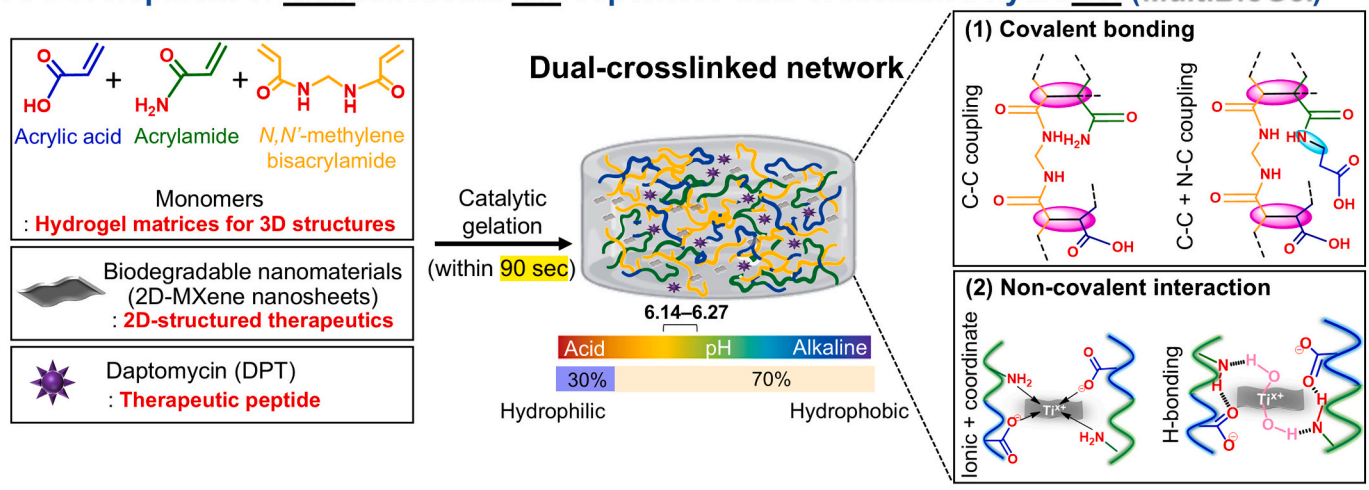

B. The MultiBioGel enabled modulation of biophysical cues for combined therapeutic effects

(1) Tunable mechanical/physicochemical properties influencing on the wound healing

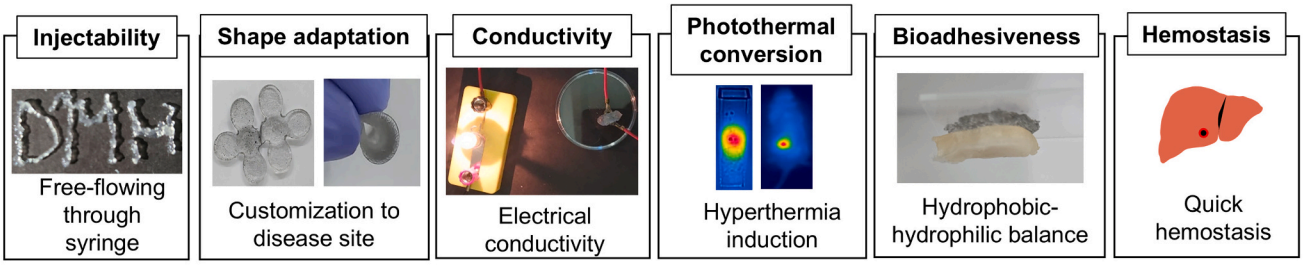

(2) Effective delivery of therapeutic payloads to enhance wound healing

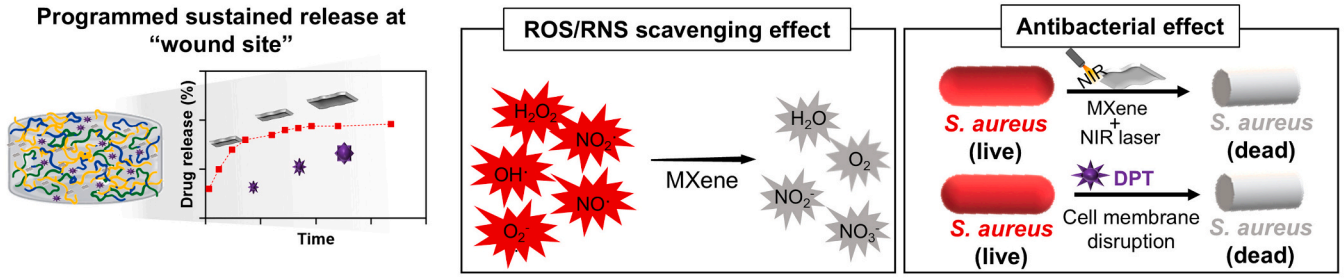

C. Enhanced bacteria-infected diabetic wound healing using MultiBioGel

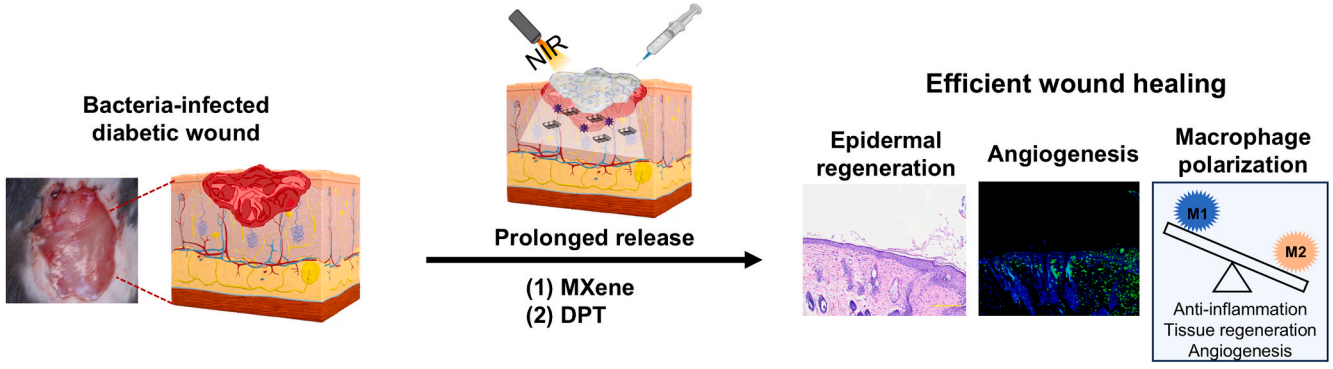

Fig. 1. Schematic of the 2D MXene-entangled terpolymer-peptide hydrogel system for healing bacteria-infected diabetic wound.

Dynamic light scattering showed a unimodal particle size distribution of 439.2 ± 105.1 nm, and the zeta potential was −5.5 ± 0.2 mV.

FE-SEM image of MXene (Fig. S4) shows orderly arranged exfoliated planes, while rough and irregular particulate depositions appear on the surface of the MAX phase. The average plane thickness in MXene is 144.7 ± 40.2 nm, confirming its nanostructure dimension.

The HR-TEM image of MXene contained the regular arrangement of 2D-sheets (planes), having the interplanar distance of 1.317 nm (Fig. S5). Such observation largely resembles those results in previous study [28].

3.3. Statistical optimization of synthesis parameters for MXene/polymer hydrogels

RSM is a statistical tool for optimizing parameters using the minimum number of experimental runs. Here, two-stage optimization process was adopted to find out the optimum synthesis conditions by performing the minimum number of experimental runs (Scheme S1). For resolution-IV design, molar ratio of AA/AAm (*A*, −), temperature (*B*, °C), amounts of MBAm (*C*, wt%), initiator content (*D*, wt%), total monomer concentration (*E*, wt%), and MXene concentration (*F*, mg/mL) were varied within ranges: 1–10, 20–40 °C, 1.5–2.5 wt%, 1–6 wt%, 10–30 wt%, and 1–5 mg/mL, respectively (Table S1). Based on software-generated combinations, hydrogels were synthesized, and ESR values were input as the response variable.

Although multiple parameters (mechanical strength, NIR light responsiveness, drug release rate) are important for therapeutic efficacy, ESR was chosen as the optimization target because it determines the hydrogel's internal network structure. ESR governs water uptake and diffusion capacity while correlating with mechanical compliance, network porosity, drug loading/release behavior, and MXene sheet distribution within the polymer matrix. Optimizing ESR allowed indirect modulation of features critical for wound healing. After ANOVA (Table S2), the three most influential parameters—*A* (monomer ratio), *E* (total monomer concentration), and *F* (MXene concentration)—surpassed the Bonferroni threshold of 17.2772 (Fig. S6A) and were selected for the FCCD study. In this case, 15 hydrogel formulations were generated based on FCCD, varying *A*, *E*, and *F* across ranges (1–10, 10–30 wt %, and 1–5 mg/mL; Table S3). The 3D response surface plots (Figs. S6B–S6D) illustrated nonlinear variable interactions. According to the final ANOVA results (Table S4), the optimum values were: AA/AAm ratio = 5.8, total monomer concentration = 21.5 wt%, and MXene concentration = 3.4 mg/mL, yielding 0.975 desirability. This design ensures balanced physicochemical and therapeutic properties, including hydrogel-tissue mechanical matching, optimized MXene loading for photothermal and antioxidant effects, and structural integrity for *in vivo* applications.

3.4. Design of hydrogel systems and elucidation of gelation mechanisms

The formation of MH occurred *via* C—C coupled chain propagation to form polymer backbone, N—C coupled transformation of –$CONH_2$ to –CONH– to allocate the *in situ* comonomer, and physicochemical entrapment of MXene (Fig. 2A). In the ^{1}H NMR spectra of DMH (Fig. 2B), the absence of $\underline{H_2}C{=}C\underline{H}$– peaks of AA, AAm, and MBAm within 5.69–6.59 ppm (Fig. S7) and appearance of –$C\underline{H_2}(\alpha)$–/>$C\underline{H}$– and –$C\underline{H_2}(\beta)$– peaks within 2.16–2.29/0.81–1.46 ppm confirmed C—C coupled polymerization of the monomers, followed by MBAm-aided crosslinking, which generated the saturated polymer backbone [29]. Such saturated sp^3 C—H specific peaks were absent from the spectra of the monomers and MBAm (Fig. S7). The inclusion of AA, AAm, and MBAm in DMH was inferred from the –COO$\underline{H}$, –$N\underline{H_2}$, and –CONH–$C\underline{H_2}$–CONH– peaks visible at 12.01, 6.92–7.17, and 4.34 ppm, respectively [30–32]. The N—H activated inclusion of AAMPPA *via* conversion of –$CONH_2$ of AAm to –CONH– in DMH was confirmed from >N$\underline{H}$ and –CONH$C\underline{H_2}$– peaks at 8.09–8.30 and 3.45–3.58 ppm [31]. For the first time, the formation of an MXene-based terpolymer moiety, instead of MXene-grafted-copolymer system, could be reported (Scheme S2). The mechanical fragility of homo-/copolymers can be compensated by synthesizing terpolymer hydrogels, which improves hydrogel structure with elevated mechanical strength and sensitivity toward physical and chemical stimuli [29]. Ti^{2+} of MXene accelerates heterolytic cleavage of $K_2S_2O_8$ to generate $SO_4^{\bullet-}$, the primary chain initiating/propagating agent. The presence of MXene accelerated both the initiation and propagation of polymer chains. Ti-complexes efficiently induce N—H activation [13]. The combination of faster radical generation and N—H activation by Ti-center of MXene resulted in faster gelation (~90 s) involving N—C coupling compared to previous reports [10]. Various types of chemical bonds (such as covalent, ionic, and coordinate) and physical interactions (such as hydrogen bonding), associated with the formation of MH, are depicted in Fig. 2C.

The overall TG plot of BH and DMH (Fig. 2D) can be divided into two ranges: the first decomposition range within 35–120 °C shows loss of hydrogen bonded water molecules and the second range within 280–480 °C is related to the combined mass loss due to acid-to-anhydride formation, amide-to-imide formation, and anhydride/imide decomposition to generate CO_2 and NH_3 [33]. DMH exhibited enhanced thermal stability compared to BH across the temperature range, likely due to chemical bonds formed between MXene, DPT, and BH during synthesis. Notably, the higher amount of residue in DMH (48.0 wt%) than that in BH (37.2 wt%) could be ascribed to the presence of thermostable MXene in DMH.

The FT-IR spectra (Fig. 2E and Table S5) of BH and MH showed peaks at 2933 and 2934 cm^{-1}, which corresponded to C—H *asym. str.* of –CH_2– and indicated C—C coupled polymerization of $H_2C{=}CH$– (observed in the ^{1}H NMR analysis). In BH, AA moiety was confirmed by peaks at 1704 and 1663 cm^{-1} from C═O *str.* of –COOH dimer and –COO^-. These peaks shifted to 1698 and 1656 cm^{-1} in MH owing to the coordinative attachment of MXene with BH moiety. This interaction was also evident from the sharpening and shifting of hydrogen bonded O–H… N—H *str.* from 3363 cm^{-1} of BH to 3407 cm^{-1} in MH. The presence of MXene in MH was confirmed by the peak at 610 cm^{-1} from C—F *def.*. The N—H activated inclusion of AAMPPA converting –$CONH_2$ of AAm to –CONH– in BH/MH was shown by peaks at 1539/1544 cm^{-1} from amide-II (N—H *def.*) of –CONH–, *i.e.,* the secondary amide.

DPT is an anionic complex lipopeptide containing Ar-NH_2, –$CONH_2$, –CONH–, indole-NH, –COOH, and –CH_2OH [34,35]. The large amounts of N—H functionalities resulted in the lowest mutually hydrogen bonded O–H… N—H *str.* at 3283 cm^{-1}. In DPT, indole moiety was confirmed from C—H *str.*, aromatic C═C *str.*, and C═C *bending* at 3069, 1450, and 741 cm^{-1} [36]. The prominent peaks of DPT appeared at 2927/2853, 1640, and 1521 cm^{-1}, attributed to C—H *asym. str.* of –CH_2–, C═O *str.* of –COO^-, and amide-II. The hydrogen bonding environment changed drastically after DPT loading. The increased population of nitrogenous functionalities after DPT loading resulted in the reduction of mutually hydrogen bonded O–H… N—H *str.* from 3407 cm^{-1} of MH to 3374 cm^{-1} in DMH. The appearance of DPT-specific peaks at 1450 and 758 cm^{-1} in DMH, attributed to aromatic C═C *str.* and C═C *bending* of indole moiety, indicated DPT loading. C═O *str.* of –COOH dimer and –COO^- peaks of MH remained unchanged after DPT loading, suggesting the non-involvement of these functional groups in covalent/coordinate bonding. This indicated ionic or hydrogen bonding during DPT loading. The superficial charge distribution of BH was key in encapsulating DPT. According to Fig. S8, the pH_{PZC} of BH is 6.24. Therefore, the surface charge of BH was cationic at pH 5.5 during synthesis. The electrostatic attraction between cationic BH and anionic DPT enabled efficient DPT loading.

Interactions among hybrid gel ingredients were elucidated by XPS analysis (Figs. 2F and S9-S12 and Table S6). The deconvoluted C 1s spectrum of MXene (Fig. S9 and Table S6) shows three peaks at binding energy (BE) = 283.32, 286.64, and 291.46 eV due to Ti—$\underline{C}$ (carbide ion), $\underline{C}$–OH (terminal OH), and –$\underline{C}$OOH (from aerial oxidation of terminal

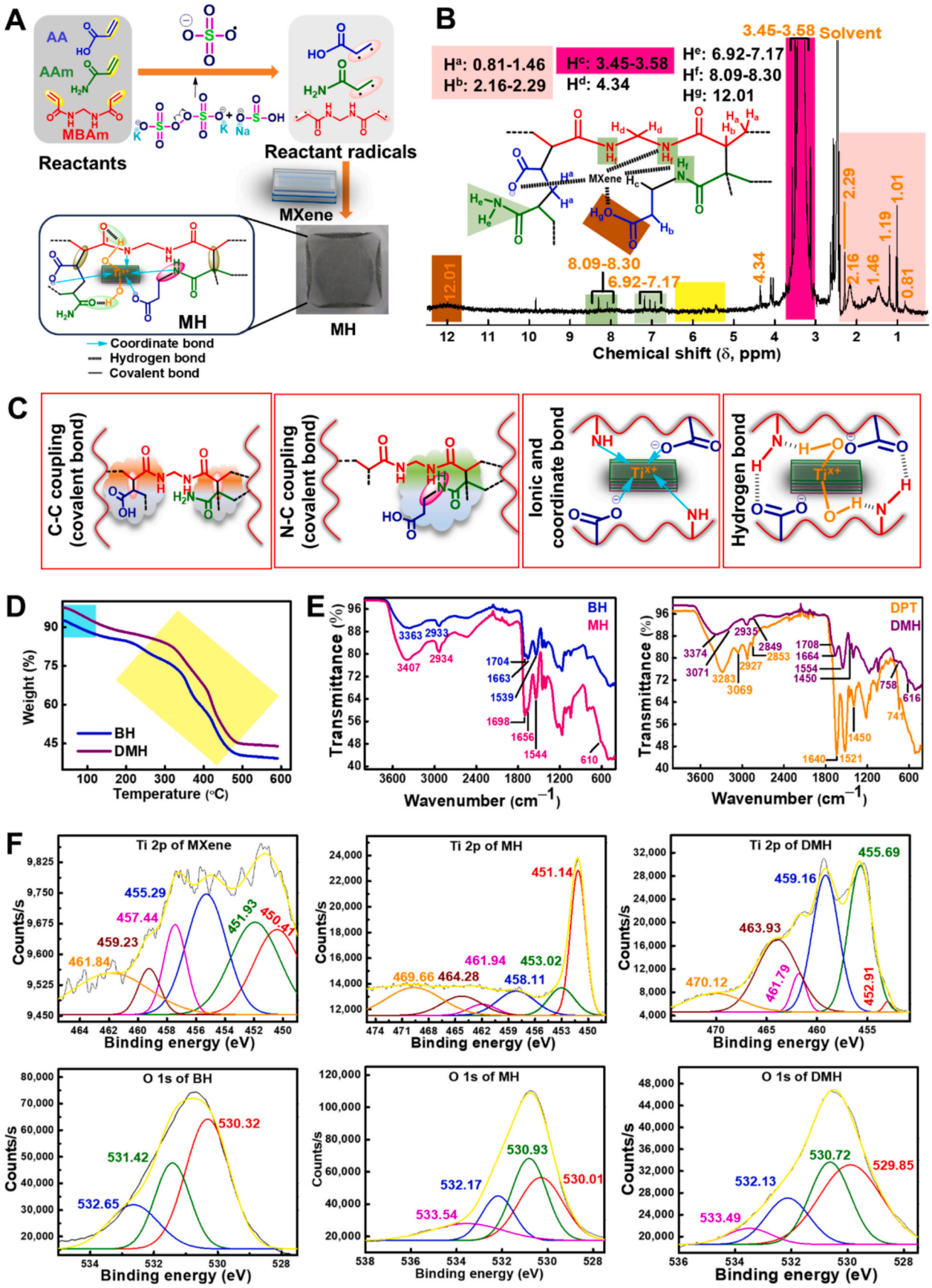

Fig. 2. Synthesis of DMH and its identification: (A) Synthetic sketch of DMH from reactants and (B) ^{1}H NMR spectrum of DMH. (C) Feasible gelation interactions within the microstructure of DMH. (D) TG plots of BH and DMH. (E) FT-IR spectra of BH, MH, DPT, and DMH. (F) XPS profiles of MXene, BH, MH, and DMH.

–OH of MXene). The O 1s spectrum of MXene shows three peaks at BE = 529.72, 530.87, and 534.24 eV attributed to O_{ad}, Ti—O of –OH terminal group, and O=C(–OH)–, respectively. The Ti 2p orbital shows three sets of doublet peaks of Ti $2p_{3/2}/2p_{1/2}$ at 450.41/457.44, 451.93/459.23, and 455.29/461.84 eV, attributed to Ti–C–T_o, Ti–C–$T_{o,\ F}$, and Ti–C–T_F (T_o, T_F, and $T_{o,\ F}$ represented –OH, F^-, and –OH + F^- terminal groups).

The deconvoluted C 1s spectra showed peaks at BE = 284.12, 287.62, and 292.22 eV in BH (Fig. S10) and 283.91, 287.68, and 291.91 eV in MH (Fig. S11), attributed to >CH_2/>CH–, O=C(–NH_2)–/O=C(–NH–)–/O=C(–OH)–/–COO^-, and shake-up satellite band of –CO–NH–CH_2–. The C 1s spectrum of MH contained two additional peaks at BE = 283.32 and 285.61 eV, related to Ti—C (carbide ion) and C–OH (terminal OH) of MXene, indicating MXene inclusion in MH. The interaction of MXene with BH during MH formation was evident from O 1s spectra of BH and MH (Fig. 2F). BH showed three peaks at BE = 530.32, 531.42, and 532.65 eV, related to O=C(–OH)–/O=C(–NH_2)–/O=C(–NH–)–, –COO^-, and O=C(–OH)–, respectively. These peaks shifted to 530.93, 532.17, and 533.54 eV in MH after MXene grafting, indicating coordinate bonding within central-Ti(IV) of MXene and –COO^- of BH as well as –OH/F^- of MXene and electrophilic C=O centers of BH. Coordinate bonding between Ti(IV) and BH was supported by Ti 2p peak increases from 450.41/457.44, 451.93/459.23, and 455.29/461.84 eV (in MXene) to 451.14/461.94, 453.02/464.28, and 458.11/469.66 eV (in MH). The absence of significant covalent bonding was confirmed by ^{1}H NMR analysis. XPS analysis indicates a strong coordinative attachment between MXene and BH.

In DMH, DPT, MXene, and BH moieties are evident from C 1s peaks of aromatic C=C, Ti—C (carbide ion), and O=C(–OH)–/O=C(–NH_2)–/O=C(–NH–)– at 281.92, 283.40, and 288.81 eV (Fig. S12), respectively. DPT loading with MH hydrogel is confirmed from the deconvoluted N 1s spectrum of DMH showing two new peaks at BE = 401.23 and 402.44 eV due to –NH_2 and –NH_3^+ of DPT with MH-specific amide nitrogen peaks. The weak ionic interaction of DPT with –OH/F^- terminal functionalities of MXene is shown by O 1s peaks shifting of O_{ad} and Ti—O of terminal –OH from 529.72 and 530.87 eV of pristine MXene to 529.85 and 530.72 eV in DMH (Figs. 2F and S9). The non-involvement of –COO^- during binding with DPT, noted in FT-IR analysis, is confirmed by XPS analysis through minimal –COO^- shifting from 532.17 of MH to 532.13 eV of DMH (Fig. 2F).

3.5. Physicochemical features of hydrogel systems

The formation of hydrogel was evident from FE-SEM images of freeze-dried samples of BH and DMH (Fig. 3A). The superficial porosity of DMH was slightly lower than BH due to the presence of MXene and DPT. The pore diameters of BH and DMH were 124 and 101 μm, respectively. FE-SEM images of oven-dried MH showed comb-like morphology (Fig. S4), indicating interpenetrating polymer network hydrogel formation *via* MXene grafting within the microstructures of BH [19].

The sol-to-gel behaviors of hydrogel structures were tested using an inversion method (Fig. 3B). Hydrogel formation is demonstrated by the AA, AAm, and MBAm reaction, and the sol-to-gel transition was confirmed in BH gel. The incorporation of MXene and DPT into BH gel did not interfere with the sol-to-gel transition. The swelling kinetics data of hydrogels at pH 7.4 and 8.5 are given in Figs. S13 and S14. Mean ESR values followed: BH < DH ≤ MH < DMH, due to hydrophilic functional groups in DPT, MXene, and DPT + MXene in DH, MH, and DMH, respectively. The mean ESR values were higher at pH 8.5 compared to pH 7.4 because at higher pH, more –COOH and O—H functionalities were deprotonated to –COO^- and —O, causing network swelling and increased water absorption. The CD of hydrogels was calculated using Eq. (2) [19]. The CD varied as BH (2.96×10^{-8}) < DMH (10.95×10^{-8}) (Fig. 3B), confirming a more compact structure in DMH.

Viscoelastic properties of hydrogel systems were analyzed by rheometer (Figs. 3C and S15). For BH, G′ value was higher than G″ up to 10 rad/s, whereas for DHM hydrogel, G′ was higher than G″ throughout the frequency range studied. These data indicate higher network fragility of BH compared to DH, MH, and DMH. A higher G′ value (notably in frequency sweep data) in MH compared to BH indicates MXene's involvement in crosslinking reaction with MBAm to strengthen the hydrogel network. DPT's presence elevated network integrity for both DH and DMH compared to BH. G′ values at 100 rad/s followed: 416.7, 791.2, 1531.8, and 1873.7 Pa for BH, DH, MH, and DMH in frequency sweep data. All hydrogel groups exhibited a shear rate-dependent decreasing pattern in viscosity. This shear-thinning behavior enables easy application on wound area through a syringe system.

Mechanical studies of all the hydrogel specimens were carried out after swelling for 0.5 and 72 h, designated as swelled and equilibrium swelling hydrogels, respectively (Figs. 3D–H and S16). The tensile stress–strain curves comprise three zones: initial elastic zone up to YP, characteristic J-shaped strain-stiffening behaviors where slope increased with strain up to breaking stress (BS) point, and post-BS zone where slope decreased with strain up to FP, followed by total fracture. Ultimate tensile strength and compressive stress values of swelled DMH were 127.5 ± 17.7 kPa and 1.2 MPa (Fig. 3E and F), substantially higher than MXene-based copolymer [16]. Young's modulus and toughness values followed: DMH > MH > DH > BH (Fig. 3G and H). These data confirmed DMH's enhanced mechanical stability compared to other hydrogels, resulting in higher stretchability (Fig. 3I). In comparison to swelled conditions (Fig. 3D), the equilibrium swelling hydrogels exhibited lower tensile stress because of the loosening of the hydrogel network (Fig. S16A) [37]. Therefore, the associated parameters of tensile stress *vs.* strain plot, such as ultimate stress, Young's modulus, and toughness (Fig. 3E, G, H, and S16C), were found to reduce in equilibrium swelling conditions. Notably, BH, DH, and MH were found to be very fragile in equilibrium swelling conditions, whereas DMH could hold its network integrity even after incubation for 72 h. However, no such drastic reduction in compressive stress of hydrogels could be observed in equilibrium swelling conditions (Figs. 3F and S16B). A supramolecular hydrogel with macroporous structure (100–200 μm pore size) showed reduced mechanical strength under moist conditions [16]. Unstable mechanical properties failed to withstand maximum wound tensile strength in moist environments, reducing efficiency in tissue engineering applications. Hydrogels exhibiting both robust mechanical strength and enduring deformation resistance at equilibrium are rarely reported. Therefore, in equilibrium, DMH may show similar compressibility with higher softness, which might be helpful in covering the wound area for a longer time in-presence of biological fluids.

Animal skin is electrically sensitive tissue, with conductivity values within 2.6 to 1×10^{-4} mS/cm [38]. Electrically conductive wound healing materials with conductivity close to human skin can promote cell adhesion, proliferation, migration, and differentiation, accelerating chronic wound healing [39]. The variation of impedance with frequency is explained in the Bode plot (Fig. S17). According to the Bode plot, the electrical conductivity values of BH/DMH were 0.0003/0.0066, 0.002/0.036, 0.012/0.219, and 0.035/1.304 mS/cm at 0.1, 1, 10, and 100 Hz, respectively (Figs. 3J and S17). The conductivity values of DMH were higher than those of BH, making it more suitable for wound healing and within the conductivity range of skin tissues. The CV plots of BH and DMH (Fig. S18) indicated that the current density of DMH was higher than that of BH at high applied potentials, demonstrating the improved conductivity of DMH. MXene-based hydrogels possess diverse conductivity values [40–42]. DMH absorbs wound exudates and transmits bioelectrical signals in response to endogenous electric fields in diabetic wounds, resulting in better proliferation, migration, and differentiation [43]. During re-epithelialization, disrupted TEP gradually re-establishes to increase electrical resistance around the wound area. Electroactive wound healing material with potential comparable to skin (15–45 mV/mm) aids rapid wound healing. DMH's potential was 41 mV/mm, within the TEP range of human skin [44]. The electroactive nature of DMH may

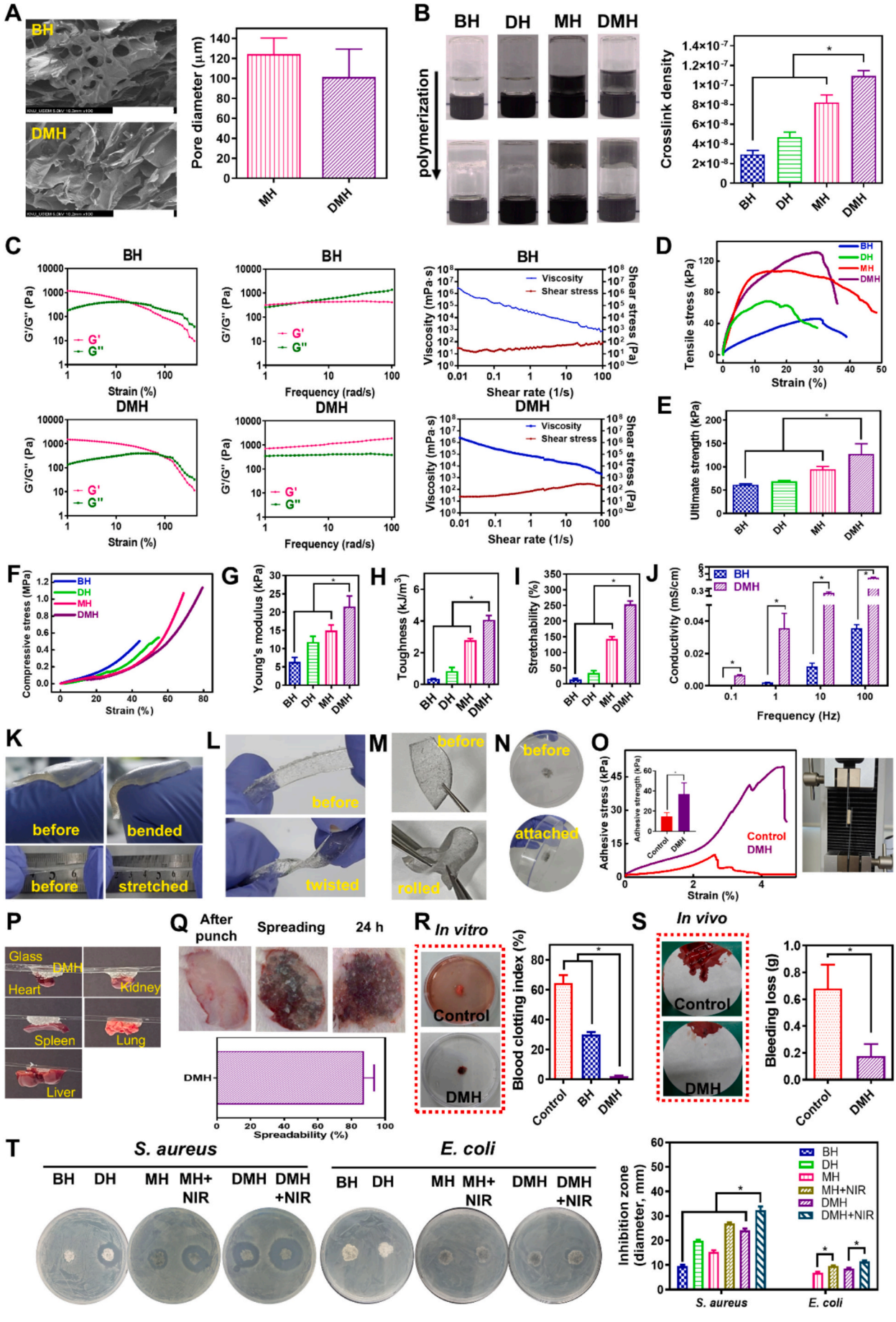

(caption on next page)

Fig. 3. Physicochemical properties of hydrogel systems: (A) FE-SEM images and the corresponding pore diameter values of MH and DMH. Scale bar: 500 μm. Each point represents mean ± SD ($n \geq 4$). *$p < 0.05$, between the indicated groups. (B) Inversion test to confirm sol-to-gel transition and CD values of BH, DH, MH, and DMH. Each point represents mean ± SD ($n = 3$). *$p < 0.05$, between the indicated groups. (C) Rheological data of BH and DMH. (D) Tensile stress and (E) Ultimate strength values of BH, DH, MH, and DMH. Each point represents mean ± SD ($n = 3$). *$p < 0.05$, between the indicated groups. (F) Compressive stress profiles of BH, DH, MH, and DMH. (G) Young's modulus values of BH, DH, MH, and DMH. Each point represents mean ± SD ($n = 3$). *$p < 0.05$, between the indicated groups. (H) Toughness values of BH, DH, MH, and DMH. Each point represents mean ± SD ($n = 3$). *$p < 0.05$, between the indicated groups. (I) Stretchability data of BH, DH, MH, and DMH. Each point represents mean ± SD ($n = 3$). *$p < 0.05$, between the indicated groups. (J) Frequency-dependent conductivity plots of BH and DMH. Each point represents mean ± SD ($n = 3$). *$p < 0.05$, between two groups. (K) Shape adaptability (with finger) and stretching capability of DMH. (L) Twisting flexibility of DMH. (M) Rolling property of DMH. (N) Attachment of DMH onto the plastic surface. (O) Bioadhesion strength of DMH with respect to porcine skin tissue and the experimental setup image of bioadhesion test. Each point represents mean ± SD ($n = 3$). *$p < 0.05$, between the indicated groups. (P) *Ex vivo* bioadhesion test of DMH with major organs. (Q) *In vivo* spreading capability of DMH on the wound skin. Images of after punch, spreading, and 24 h post-adhesion are shown. Each point represents mean ± SD ($n = 3$). (R) *In vitro* hemostatic assay of BH and DMH. Each point represents mean ± SD ($n = 3$). *$p < 0.05$, between the indicated groups. (S) *In vivo* hemostasis test of DMH in the liver of rat. Each point represents mean ± SD ($n = 3$). *$p < 0.05$, between the indicated groups. (T) *In vitro* antibacterial studies against *S. aureus* and *E. coli*. Images of antibacterial test on the plate and diameter plot of inhibition zone. Each point represents the mean ± SD ($n = 3$). *$p < 0.05$, between the indicated groups.

enhance wound healing efficacy.

Bending, stretching, twisting, rolling, and attaching properties of DMH in air and underwater conditions were demonstrated in Figs. 3K–3N and S19. DMH adopted the shape of the finger when bent and regained its original shape when straightened. It stretched almost twice its initial length, demonstrating stretchability. DMH was flexibly twisted, rolled up, and attached to plastic petri-dishes so firmly it remained attached when tilted perpendicular. The bending, twisting, rolling, and adhesion of DMH with glass and porcine skin were also studied in underwater conditions. Like air, all the above-mentioned properties could be observed in underwater conditions (Fig. S19), justifying the utility of DMH in moist wound conditions.

The tissue adhesion property of the hydrogel system offers advantages for wound healing through proper fixing of therapeutics on the wound. For assessing the adhesive strength of DMH in swelled and equilibrium swelling conditions, lap shear tests (Figs. 3O, S20, and S21) were carried out with DMH (fixed in glass slide) and porcine skin tissue (fixed in glass slide) and compared with the adhesive stress of only porcine skins (control) [45]. DMH exhibited a significantly higher adhesion strength of 37.0 ± 9.0 and 40.0 ± 1.9 kPa in swelled and equilibrium swelling conditions, respectively, compared to 14.6 ± 3.2 kPa of the control group (porcine skin) ($p < 0.05$). Moreover, in equilibrium swelling conditions, DMH could sustain a strain (%) up to 40 % compared to only 4.3 % in swelled conditions, indicating the stronger bioadhesion of DMH in underwater conditions.

Bioadhesion mechanisms of DMH to porcine skin were elucidated by FT-IR analysis (Fig. S22) of tissue/DMH composite. To analyze the superficial interaction between tissue and DMH, two conditions of tissue/DMH composites were considered for FT-IR analysis: (a) tissue facing the diamond of ATR (Tissue–DMH) and (b) DMH facing the diamond of ATR (DMH-Tissue). These spectra were compared with individual spectra of tissue and DMH. Significant modification in hydrogen bonding was observed in tissue/DMH composites compared to individual tissue and DMH. The sharp non-hydrogen bonded N—H and O—H *str.* peaks at 3408, 3298, and 3082 cm^{-1} of tissue either vanished or became broad, indicating hydrogen bonding formation. The mutually hydrogen bonded N–H…O–H *str.* peak at 3374 cm^{-1} of DMH broadened and shifted to 3363/3215 cm^{-1} in DMH-Tissue group (Figs. 2E and S22). Except for these changes, the FT-IR spectra of tissue, DMH, and tissue/DMH composites appeared similar. Therefore, hydrogen bonding interaction is the primary chemical interaction behind DMH's strong adhesion to skin tissue.

DMH exhibited appreciable adhesion to *ex vivo* organs, such as the heart, kidney, spleen, lung, and liver (Fig. 3P). These robust adhesive properties suggest potential therapeutic applications in treating diverse organ injuries, as demonstrated by its strong adhesion to heart, kidney, spleen, lung, and liver tissues.

The *in vivo* spreadability of DMH was studied by applying hydrogel onto mouse wounds (Fig. 3Q). After 24 h, most hydrogels remained with 83.5 % retention compared to the initial application. These properties showed convenient spreadability and retention of DMH in wounds.

A blood-clotting assay evaluated the hemostatic potential of DMH (Fig. 3R and S). More blood was dispersed in DW for the control group (cotton gauze) *versus* DMH (Fig. 3R), indicating no blood coagulation for the control. The water around DMH was almost colorless, confirming excellent coagulation capacity. BCI data quantified the coagulation properties of cotton gauze (control), BH, and DMH. BCI values of control, BH, and DMH were 64.4 %, 30.1 %, and 2.1 %, respectively, showing enhanced blood-clotting effects. Hemostasis is the first critical step in wound healing. The *in vitro* hemostasis potential of DMH was further evaluated by observing the clotting time of recalcified rat blood (treated with trisodium citrate) on the surface of BH and DMH in comparison to control (Fig. S23). The clotting time was found to reduce significantly from 10.4 ± 0.3 min of control to 6.2 ± 0.4 and 1.0 ± 0.1 min of BH and DMH, respectively. Such data inferred the superior hemostatic performance of DMH.

The *in vivo* hemostatic effects of hydrogels were demonstrated using a rat liver slice resection wound bleeding model (Fig. 3S). DMH showed significantly lower bleeding compared to the control group. Mean blood loss values were 0.68 and 0.18 g for control and DMH, respectively. These results showed DMH's excellent potential for hemostasis. Therefore, by combining the *in vitro* and *in vivo* hemostasis data, it can be concluded that DMH hydrogel has high blood clotting capability for wound healing.

The hemolysis data in Fig. S24 showed values of 2.2 % and 0.4 % for BH and DMH, respectively, compared to 92.7 % for positive control. As <5 % hemolysis rate indicates nontoxicity [22], both BH and DMH can be considered as hemocompatible materials.

3.6. *In vitro antibacterial and wound healing mechanisms*

Owing to the high risk of bacterial infection in diabetic wounds, DPT was selected as an antimicrobial peptide to enhance wound healing [46]. DPT is highly effective against gram-positive bacteria, such as *S. aureus* [46]. DPT's antibacterial mechanisms involve permeabilization and depolarization of bacterial cell membranes, disrupting membrane function and inhibiting protein, DNA, and RNA synthesis [47,48]. The antibacterial performances of hydrogels (BH, DH, MH, and DMH) with NIR light were evaluated by measuring DIZ around samples on agar plates with *S. aureus* suspension (Fig. 3T). BH showed feeble antibacterial effects due to $–CONH_3^+$ moieties of AAm. The $–CONH_3^+$ ion of BH increased the probability of interaction with the negatively charged substances of bacterial cells, such as proteins, fatty acids, and phospholipids, thereby increasing the permeability of BH through the bacterial cell membranes, leading to cell death [49]. In DH, the significant broadening of the inhibition zone could be attributed to the combined antibacterial effects of BH and DPT. In MH, the significant enlargement of DIZ, compared to that in BH, could be related to the superior antibacterial efficacy of MXene, originating from Ti^{n+} ions, which enhanced the electrostatic interactions among the negatively charged bacterial

cell components. Moreover, the layered structure of MXene can physically damage bacterial cell membranes. Specifically, its open-stacked 2D nanosheet structure acts as a nano-knife, disrupting bacterial outer membranes and contributing to its intrinsic antibacterial activity [50]. Therefore, in DMH, the combinatorial effects of DPT and MXene increased DIZ significantly compared to other hydrogels. Photothermal effects by NIR light irradiation provided additional antibacterial activity with DMH. MXene generates localized heat through plasmonic photothermal conversion, which further disrupts bacterial membrane integrity. This thermal effect likely enhances membrane permeability, facilitating deeper penetration and improved efficacy of DPT. Local heat from NIR light irradiation induced bacterial cell death [51], as shown in MH + NIR and DMH + NIR groups.

To further validate this conclusion, a bacterial colony-counting assay was done. According to Fig. S25A, the number of bacterial colonies followed the order: BH > DH > MH > MH + NIR > DMH > DMH + NIR. Notably, bacterial growth was almost completely suppressed in the DMH + NIR group. These findings demonstrated that the individual antibacterial effects of MXene and DPT were not sufficient to fully eliminate *S. aureus*, yet their combination, particularly under NIR light irradiation, could generate superior antibacterial activities.

We also acquired the SEM images of *S. aureus* to explain the antibacterial mechanism *via* observing their morphological changes (Fig. S25B). For *S. aureus*, it retained spherical morphology with smooth surfaces for control group. However, bacteria treated with DPT and/or MXene-loaded hydrogels exhibited clear morphological disruption. Notably, in the DMH + NIR group, the bacterial cells appeared severely deformed or bisected, suggesting extensive membrane damage caused by the combined effects of DPT, MXene, and NIR light.

Next, *in vitro* antibacterial potential of designed hydrogel systems was assessed in *E. coli*. DPT is known to have insignificant antibacterial efficacy against *E. coli* [52]. This could be ascertained from observing the DIZ values of *E. coli* for DPT and hydrogel specimens (Fig. 3T). No DIZ could be observed for BH and DPT. However, due to the antibacterial effect of MXene combined with NIR light, MH < MH + NIR and DMH < DMH + NIR patterns are shown. The insignificant improvement in DIZ values of DMH and DMH + NIR compared to MH and MH + NIR, respectively, could be explained from the inactivity of DPT in killing gram-negative *E. coli*. Overall, the DIZ values for *E. coli* were found to be significantly lower than those of *S. aureus*. Similar observation could be visualized from the colony growth experiments of *E. coli* (Fig. S26A). In contrast to *S. aureus*, *E. coli* showed a slightly different response, as DPT alone had negligible antibacterial effects. Instead, antibacterial activity was primarily attributed to MXene and NIR light irradiation. The layered structure of MXene is the key of its antibacterial efficacy as described previously [50,53]. Consistent with this, FE-SEM images (Fig. S26B) showed clear signs of membrane disruption in *E. coli* treated with MH, MH + NIR, DMH, and DMH + NIR groups.

The *in vitro* photothermal transducing test of hydrogels was performed by measuring their temperature increase during NIR light irradiation (Figs. 4A and S27). The *in vitro* photothermal conversion studies were conducted in cuvettes. The ΔT values for BH and DH were 3.0 ± 0.1 and 3.0 ± 0.2 °C, respectively, showing insignificant improvement in photothermal conversion. Thus, DPT's contribution to photothermal efficiency was negligible. For DW, ΔT was negligible, indicating weak photothermal property of BH, consistent with previous findings [54]. In MH, ΔT increased to 12.0 ± 0.3 °C, significantly higher than BH and DH. The encapsulation of MXene in BH introduced photothermal conversion property in MH, making MXene the primary photothermal agent. Such photothermal behavior could be attributed to the intrinsic structural feature. The black color and rough surface morphology of the 2D MXene nanosheets allow broad-spectrum light absorption (UV–Vis–NIR), enabling efficient light-to-heat conversion—a phenomenon known as the plasmonic effect [55,56]. This structural property explains the notable temperature increase observed under 808 nm NIR light irradiation in MXene-containing hydrogels, such as MH and DMH. The ΔT was 12.3 ± 0.3 °C in DMH. No statistical difference in ΔT between MH and DMH showed DPT's insignificant contribution to DMH's photothermal potential. The elevated local temperature (ΔT of 12.3 ± 0.3 °C) promotes accelerated wound healing through enhanced cell proliferation, increased angiogenesis, and improved antibacterial activity [57,58]. The photothermal conversion efficiency (η%) of DMH was measured using a reported method [59]. DMH's η% was 73.3 % (Fig. S27A), significantly higher than reported hydrogels [60,61]. DMH's photothermal conversion reproducibility was studied through repeated heating and cooling cycles by laser on/off for 5-min cycles (Fig. S27B). The fifth trial's ΔT value was 94.8 % relative to the first NIR light application, indicating preservation of the photothermal conversion nature even after repeated heating–cooling cycles.

DPT release profile from the DMH was explored in buffered conditions at pH 6.2, 7.4, and 8.5 (Fig. 4B). Although the wound microenvironmental pH varies by type, that of chronic infected wound ranges mostly between 7.42 and 8.90 [62]. Sustained release patterns of DPT were observed from DMH in pH 7.4 and 8.5. The released amounts (%) of DPT from DMH at pH 7.4 and 8.5 after 25 days of incubation were 79.4 % and 78.3 %, respectively. In both pH values (7.4 for normal physiological pH and 8.5 for wound environment), sustained DPT release profiles were accomplished, potentially providing prolonged therapeutic efficacies in the wound site. The release test was also performed at pH 6.2, comparable to the pH_{PZC} of DMH. Here, significantly lower drug release was observed compared to pH 7.4 and 8.5, as the surface of DMH possesses equal positive and negative charges at pH = pH_{PZC}. Therefore, fewer negative charges and more positive charges compared to pH 8.5 resulted in lower electrostatic repulsion with negatively charged DPT and more sustained release.

The drug release exponent (n) was obtained from the slope of $\ln(M_t/M_\infty)$ *vs.* $\ln(t)$ plot. The value of n was found to be 0.82 (Fig. S28), which fell in the region of anomalous transport (non-Fickian transport mechanism, $0.45 < n < 0.89$) [23]. Such data inferred that drug release was achieved by drug diffusion, gel swelling, and gel erosion processes [63].

ROS generation is elevated in wound environments, and oxidative stress increases with bacterial infections. Excessive ROS accumulation can trigger inflammation, cellular damage, suppressed tissue regeneration, and delayed wound healing [12]. H_2O_2, $^{\bullet}OH$, and $O_2^{\bullet-}$ exhibit the strongest adverse impact. We studied the time-dependent scavenging potential of MXene, BH, DH, MH, and DMH toward these radicals (Fig. 4C and D) and the results were compared with that of Asc (antioxidant agent). For H_2O_2, we applied $TiOSO_4$ to produce a yellow color with residual H_2O_2. BH showed 29.3 ± 1.2 % H_2O_2 scavenging ratio at 72 h (Fig. 4D). No significant improvement in H_2O_2 scavenging was observed for DH, indicating negligible contribution of DPT in ROS scavenging. MXene exhibited stronger H_2O_2 scavenging (49.9 ± 1.1 %) than BH and DH. The H_2O_2 scavenging phenomenon of MXene has been documented elsewhere [12,64,65]. In MH, the combined effects of BH and MXene resulted in higher H_2O_2-scavenging of 67.2 ± 0.9 %. Like MH, DMH possessed similar H_2O_2-scavenging, suggesting insignificant contribution of DPT. We studied time-dependent scavenging effects against $^{\bullet}OH$ and $O_2^{\bullet-}$. $^{\bullet}OH$ scavenging was evaluated by TMB and MB assays. $O_2^{\bullet-}$ scavenging capability was assessed by NBT-based assay. In both ROS types, similar trends were observed at 72 h with respect to H_2O_2 scavenging, and scavenging potential varied as follows: BH = DH < MXene < MH = DMH. The negligible ROS scavenging capacity of DPT toward $O_2^{\bullet-}$ and $^{\bullet}OH$ was evidenced by an insignificant increase in scavenging ratio (%) from BH and MH to DH and DMH. The RNS scavenging activity was evaluated using ABTS and DPPH assays (Fig. 4D). At 72 h, a similar trend was observed, with BH and DH showing the lowest values, followed by MXene, and MH and DMH showing the highest values. In this experimental condition, Asc (one of frequently used antioxidant agents) group had higher scavenging ratios rather than control group, but lower than DMH group in all related assays.

The radical scavenging ability of MXene and DMH was confirmed by

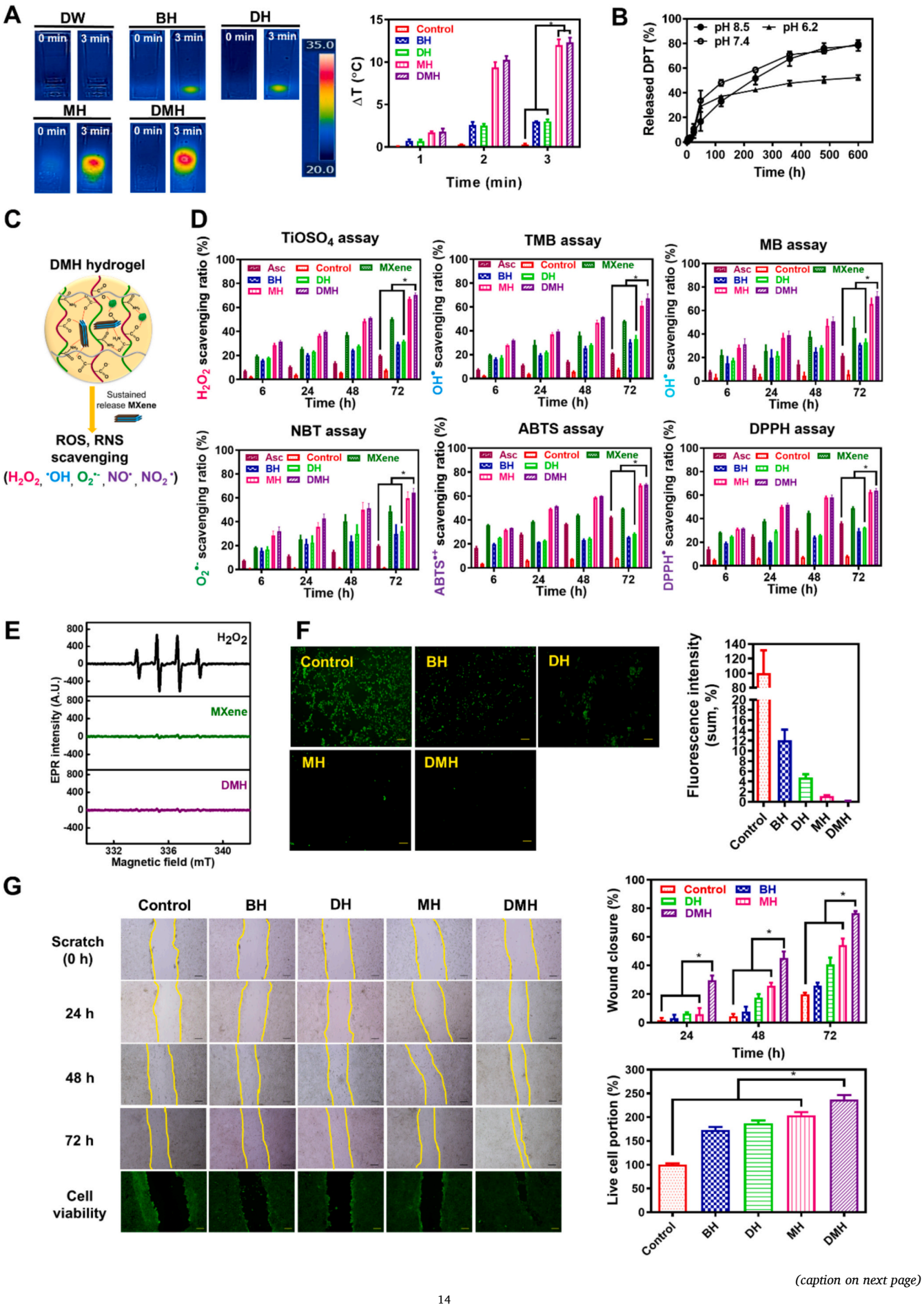

(caption on next page)

Fig. 4. *In vitro* photothermal, ROS scavenging, and wound healing studies. (A) Photothermal studies of control (*i.e.,* DW), BH, DH, MH, and DMH. Each point represents mean ± SD ($n = 3$). *$p < 0.05$, between the indicated groups. (B) Release test of DPT at pH 6.2, 7.4, and 8.5. Each point represents mean ± SD ($n = 3$). (C) Schematic of the ROS/RNS scavenging mechanism of DMH. (D) ROS/RNS scavenging potential of Asc (antioxidant), control, MXene, BH, DH, MH, and DMH. Each point represents mean ± SD ($n = 3$). *$p < 0.05$, between the indicated groups. (E) EPR studies of MXene and DMH. (F) Intracellular ROS scavenging potential of BH, DH, MH, and DMH on NIH3T3 cells using DCFH-DA probe. Scale bar: 200 μm. Fluorescence intensity plot is shown. Each point represents mean ± SD ($n = 3$). *$p < 0.05$, between the indicated groups. (G) Intracellular wound healing and live/dead fluorescence imaging of BH, DH, MH, and DMH on NIH3T3 cells. Scale bar: 200 μm. Each point represents mean ± SD ($n = 3$). *$p < 0.05$, between the indicated groups.

EPR analysis (Fig. 4E). The strong EPR signal of $^{\bullet}OH$ from H_2O_2 solution disappeared completely with MXene and DMH. Therefore, the higher $^{\bullet}OH$ scavenging ability of DMH, originating from MXene, could be ascertained.

The ROS-scavenging capability of MXene is closely related to the presence of redox-active Ti^{2+}/Ti^{3+} layers within its 2D structure. To confirm this mechanism, we evaluated the ability of MXene to scavenge $^{\bullet}OH$ using a modified H_2O_2/Fe^{2+} assay followed by XPS analysis of the residual MXene powder (Fig. S29). The deconvoluted Ti 2p peaks shifted significantly toward higher BEs, indicating the oxidation of Ti^{2+}/Ti^{3+} centers of MXene to Ti^{4+}. Specifically, new peaks observed at 458.73 and 464.56 eV correspond to the Ti 2p orbitals of TiO_2 nanoparticles, suggesting partial oxidation of MXene during reaction [66,67]. Mechanistically, in acidic environments, H_2O_2 typically reacts with Fe^{2+} to produce $^{\bullet}OH$ *via* Fenton chemistry. However, in presence of MXene, Ti^{2+}/Ti^{3+} centers preferentially reacted with $^{\bullet}OH$ to mitigate the oxidative stress. These findings provided direct evidence that the titanium centers in MXene actively contributed to ROS scavenging by serving as redox mediators.

To examine the intracellular antioxidant properties of hydrogels, DCFH-DA probe was utilized (Fig. 4F). DCFH-DA is consumed by cells and then converted to DCFH *via* cleaving of acetyl groups by cellular esterase. Oxidized DCFH (2′,7′-dichlorofluorescein) emits green fluorescence in the presence of H_2O_2 [68]. The intensity of green fluorescence directly correlates with H_2O_2 concentration (representative ROS) [12]. The strong green fluorescence observed from the positive control group after 24 h of incubation with H_2O_2 indicated the highest H_2O_2 concentration in cells. The intensity of green fluorescence decreased in order: control > BH > DH > MH > DMH. Green fluorescence was almost absent in the DMH group, suggesting its highest ROS scavenging capacity. These data showed DMH's excellent antioxidant properties in NIH3T3 cells.

The *in vitro* wound healing studies were conducted to examine NIH3T3 cell migration after scratching. The migration rates of NIH3T3 cells were higher in all the hydrogel samples (BH, DH, MH, and DMH) compared to those of the control after 72 h (Fig. 4G). Maximum migration occurred in the DMH group, showing its highest wound-healing effect. After 24 h, negligible migration appeared for control and BH, while wound closure (WC, %) values were 6.2 %, 6.1 %, and 29.7 % for DH, MH, and DMH, respectively. At 48/72 h, WC values (%) were 4.5/19.9 %, 7.7/25.9 %, 17.6/40.6 %, 25.8/54.3 %, and 45.3/76.7 % for control, BH, DH, MH, and DMH, respectively. These data demonstrated DMH's superior wound-healing efficiency [26].

The live/dead assay images in NIH3T3 cells and quantitative data are shown in Fig. 4G. The fluorescence microscopic images showed intense green fluorescence (live portion) for control and all hydrogels, confirming their biocompatibility toward NIH3T3 cells. The quantitative estimation showed relative live cell portion ratios of BH, DH, MH, and DMH were 1.7, 1.9, 2.0, and 2.4 times compared to control. Red fluorescence (dead portion) was negligible for all samples. After 72 h incubation, cell migration was fastest for DMH, indicating excellent wound healing effect.

3.7. *In vivo diabetic wound healing efficacies*

Wound healing potential and mechanisms were elucidated in non-infected diabetic mice and *S. aureus*-infected diabetic mouse models (Figs. 5, 6, and S30–S37). Wound healing capabilities of hydrogel systems were evaluated in diabetic mouse models according to the therapeutic schedule (Fig. 5A). On day 2, no significant wound closure was observed for all groups except DMH + NIR (9.6 % closure). As the experiment progressed, wound areas of DMH/DMH + NIR groups reduced rapidly, showing 45.9/65.2 %, 67.1/90.0 %, and 78.6/96.9 % wound closures at days 4, 7, and 9, respectively (Fig. 5B). The day 9 macroscopic images showed that the DMH + NIR group's wound was almost completely healed. In contrast, partial wound diameters remained visible for the other groups. These data showed the excellent wound healing of DMH with NIR light irradiation. No significant body weight change was observed (inset of Fig. 5B) in all the groups from day 0 to 9, indicating the absence of toxicity to mice.

MH and DMH groups were irradiated with NIR light on days 0, 2, 4, and 7. Both groups showed sharp temperature increases (Fig. 5C). The ΔT for the first trial was 14.5 and 14.4 °C for MH + NIR and DMH + NIR, respectively. The ΔT recorded was 12.3 and 15.0 °C in MH + NIR and DMH + NIR groups for the final trial, respectively, showing the conservation of superior photothermal properties of MXene-loaded hydrogels during testing.

The histological status of wound tissues was analyzed by H&E and MT staining (Fig. 5D). In H&E staining, nuclei and cytoplasm appear blue and pink, while in MT staining, collagen, cytoplasm, and nuclei are blue, red/pink, and black/dark brown, respectively [12,69,70]. To understand the wound nature, we selected two areas for H&E staining: the wound edge (marked with a black box) and the wound center (marked with a red box). Whole mount view results revealed that wounds in the control and DPT groups were not fully covered, while the MH group had a small epidermis defect. For MH + NIR, DMH, and DMH + NIR groups, the epidermis was connected without defective areas (Fig. S30). In the DMH + NIR group, uniform epidermis thickness and hair follicle formation were observed owing to the progression from the proliferation to remodeling phase. In the control group, epidermal thickness was thick due to wound stretch and proliferation but significantly reduced in the hydrogel group (Fig. S31). The epidermal thickness in DMH + NIR group was the lowest and similar to normal skin tissue, confirming its wound healing efficacy. MT staining showed inflammatory cell infiltration with multiple MT-negative areas in control, DPT, and MH groups, while the MH + NIR group showed thick collagen with MT-positive staining. The DMH + NIR group showed homogeneous MT-positive collagen in regular arrangement, indicating a transition to the remodeling phase. This regular collagen deposition and hair follicle regeneration support the highest therapeutic efficiency of the DMH + NIR group [12,16].

Polarization of macrophages from anti-inflammatory M2 to pro-inflammatory M1 phenotypes in diabetic environments inhibits natural wound healing [71]. To achieve rapid healing, polarization from M1 to M2 phenotype (angiogenesis) is essential. To assess M2-to-M1 phenotype ratios, IF staining of skin tissues was performed with CD206 and CD68 Abs, indicating M2 and M1 phenotypes, respectively. CD68 population reduced from control to DMH + NIR, while the opposite occurred for CD206 staining (Fig. 5D). The CD206/CD68 ratio followed: DMH + NIR > DMH = MH + NIR > MH > DPT > control (Fig. S32), confirming successful M1 to M2 polarization in the DMH + NIR group.

The *in vivo* toxicity of hydrogels was evaluated by H&E staining of vital organs (Fig. S33). No significant histopathologic changes were observed in these organs across treated groups compared to control, indicating no harmful damage. DMH can be considered biologically safe when administrated as a topical treatment [72]. Further, AST, ALT, ALB,

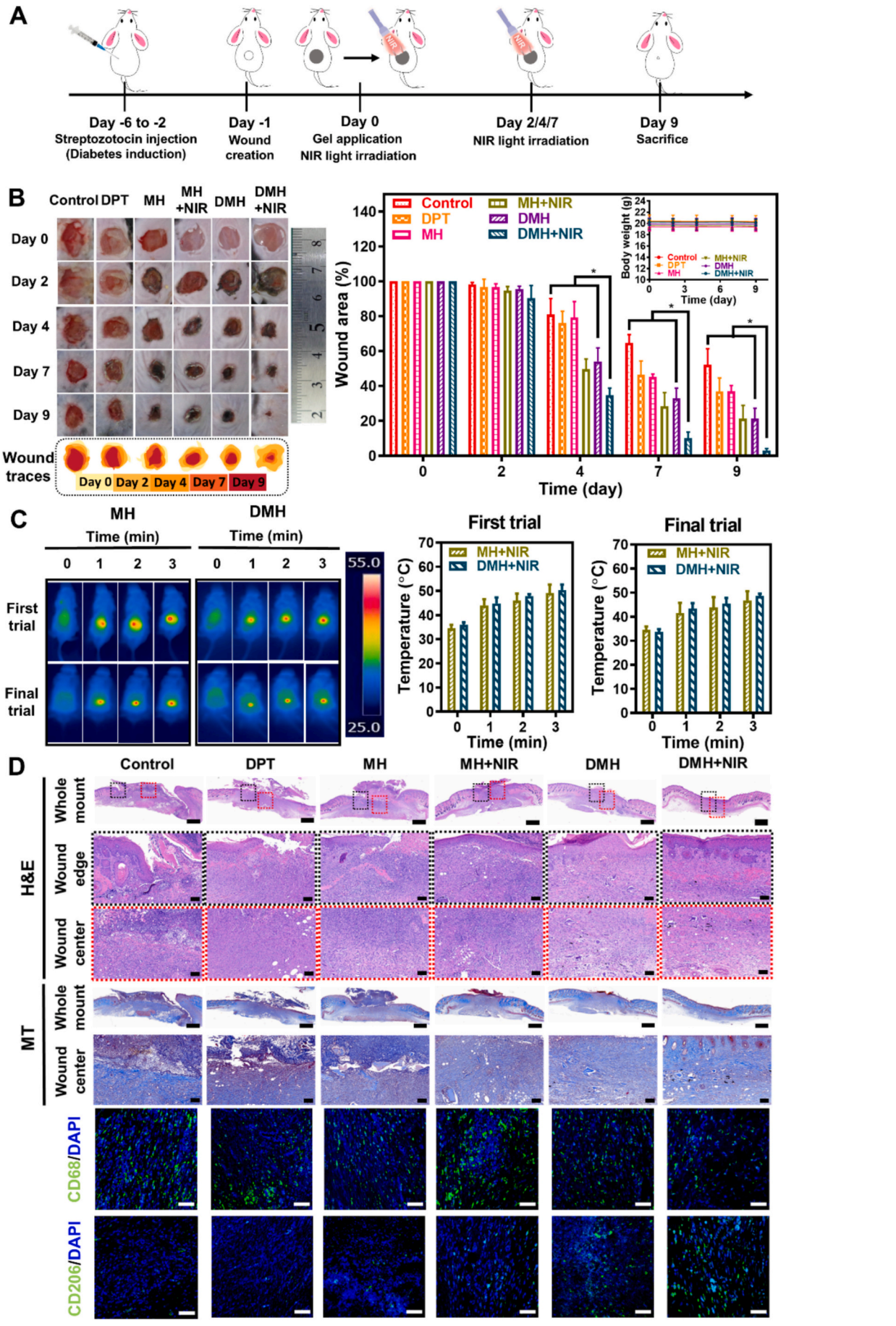

(caption on next page)

Fig. 5. *In vivo* wound healing experiment in non-infected diabetic mouse models. (A) Therapy schedule illustration. (B) Optical images of wounds, wound traces, quantitative estimation of wound healing (%), and body weight of mice (inset) on day 0 to 9 of the groups: control, DPT, MH, MH + NIR, DMH, and DMH + NIR. Each point represents mean ± SD ($n \geq 5$). *$p < 0.05$, between the indicated groups. (C) Thermal images and temperature profiles of photothermal study. Each point represents mean ± SD ($n \geq 5$). (D) H&E, MT, and IF (CD68 and CD206) staining of the skin on day 9. Scale bar: 1 mm (for whole mount images) and 100 μm (for the others).

and BUN levels in plasma samples of all mice groups were measured to evaluate hepatic and renal functions (Fig. S34). The AST, ALT, ALB, and BUN levels of the treated groups were found similar to the control group. Therefore, the systemic safety of the therapeutical hydrogels was confirmed through histological and blood biochemistry analyses.

The therapeutic strategy of hydrogel systems in bacteria-infected diabetic wound healing experiments is depicted (Fig. 6A and B). Due to bacterial growth in the wound region, natural healing was slower compared to un-infected mice (Fig. 5), shown by minimal healing in the control group up to day 6 (Fig. 6C). Up to day 10, no significant wound closure occurred for DPT and MH groups *versus* the control group. Although MXene shows antibacterial activity through Ti^{4+} ions and electrostatic interactions with bacterial cells, this mechanism alone was insufficient to inhibit bacterial proliferation and promote wound closure. MXene monotherapy's limited efficacy suggests the need for combining additional antibacterial agents for optimal healing. Similarly, the DPT group's poor healing efficiency confirmed inadequate antibacterial efficacy against bacteria-infected diabetic wounds. The significant improvement in wound healing of MH + NIR group (50.2 % healing on day 10) was related to hyperthermia-boosted antibacterial effects. The DMH + NIR group proved the best therapeutic, resulting in 90.1 % wound closure on the final day. The combined effects of MXene + NIR (photothermal, angiogenesis, and ROS scavenging abilities) and DPT (antibacterial property) in the hydrogel network made DMH + NIR the optimal therapeutic. These data confirm DMH with NIR light's excellent healing efficacy for diabetic and bacteria-infected wounds. Like the previous experiment, no significant change in mice body weights occurred (inset of graph in Fig. 6C) in all groups, indicating an absence of significant toxicity.

As shown in Fig. 6D, MH and DMH groups showed temperature elevations. During the first/final trials, ΔT values were 16.7/16.0 and 18.4/17.9 °C for MH + NIR and DMH + NIR groups, respectively. Although ΔT values reached ~18 °C, the NIR light was applied briefly, with heating localized to the wound area. Studies have demonstrated that controlled photothermal pulses in the 45–50 °C range enhance antibacterial efficacy through thermal disruption of bacterial membranes [16], while stimulating beneficial cellular responses like angiogenesis and macrophage polarization [9,12]. The hydrogel matrix, with its embedded 2D MXene network, enabled efficient photothermal conversion and localized heat confinement, preventing systemic overheating or damage to adjacent tissues.

According to *in vivo* antibacterial efficacy studies (Fig. 6E), a significantly reduced *S. aureus* colony in the DMH + NIR group was shown compared to other groups. These data indicated the combined effects of MXene, DPT, and NIR light in inducing antibacterial properties.

The wound healing effect was explored by H&E and MT staining of skin tissues (Fig. 6F). Wide open wounds were observed in the H&E staining of the control group, and less but still open wounds were observed in the DPT, MH, MH + NIR, and DMH groups. The DMH + NIR group did not show epidermal defects as well as exhibited enhanced wound healing, including epidermal maturation and increased hair follicles. MT-stained images of the DMH + NIR group showed a uniformly distributed collagen layer along the epidermis, confirming superior wound healing. *In vivo* histological analysis confirmed the absence of thermal necrosis in normal tissue or delayed healing, supporting that our system provided safe and transient hyperthermia, which promoted wound sterilization and tissue regeneration.

IF staining of VEGF and CD31 evaluated the stimulatory effect of therapeutics on angiogenesis in skin tissues (Fig. 6F) [24]. VEGF and CD31 indicate blood vessel generation and neovascularization, essential for supplying nutrients and oxygen to newly formed tissues during wound healing [12,24]. Notably, MXene's photothermal effect under NIR light irradiation can further stimulate blood perfusion and angiogenic signaling by inducing localized mild hyperthermia, which has been reported to enhance VEGF expression and vascular remodeling [73,74]. Consistent with this, the intensity of green fluorescence signals of VEGF and CD31 increased from control to therapeutic groups, reaching a maximum in the DMH + NIR group, indicating the strongest angiogenesis. Quantitatively (Fig. S35), average VEGF and CD31 expression levels were ordered: control ≤ DPT ≤ MH < MH + NIR < DMH < DMH + NIR. These data showed elevated vascular density in the DMH + NIR group, justifying remarkable angiogenesis in wound tissues for effective repairment of bacteria-infected diabetic wounds. Polarization of M1 to M2 phenotype was confirmed through IF staining (CD68 and CD 206) and fluorescence intensity ratios of CD206/CD68 (Figs. 6F and S36). Immunofluorescence analysis showed the DMH + NIR group had minimal CD68 expression (M1 marker) with maximal CD206 expression (M2 marker), yielding the highest CD206/CD68 fluorescence intensity ratio. This polarization profile indicates optimal macrophage phenotype switching from pro-inflammatory M1 to anti-inflammatory M2 states, essential for wound healing. MXene's antioxidant capacity reduces ROS-induced stress, supporting this phenotypic transition. Furthermore, DPT not only reduced bacterial burden but also helped suppress pro-inflammatory cytokines [75], contributing to a favorable microenvironment. The enhanced M2/M1 ratio in DMH + NIR treatment suggests successful modulation of inflammatory response toward a pro-regenerative environment. Collectively, these enhancements in angiogenesis and macrophage polarization contributed to accelerated wound closure and effective tissue remodeling, highlighting the therapeutic relevance of DMH hydrogel. Moreover, by facilitating a rapid transition from inflammation to proliferation, the hydrogel promoted neovascularization and tissue regeneration, resulting in rapid healing outcomes.

Compared to natural polymer-based hydrogel systems such as hyaluronic acid, chitosan, and gelatin [76–79], MultiBioGel exhibited enhanced mechanical durability, long-term stability under moist wound conditions, and more effective antibacterial activity owing to the combinational effects of MXene and DPT under NIR light irradiation. These integrated advantages make MultiBioGel a highly promising alternative for managing complex chronic wounds.

The *in vivo* toxicity of hydrogels was evaluated by blood biochemistry profiles, such as AST, ALT, ALB, and BUN (Fig. S37). Although the mean ALT level of the DMH + NIR group was lower than that of the control group, the difference was insignificant. The DMH + NIR group did not show statistical differences in blood biochemistry data compared to those of the control group, indicating proper hepatic and renal functions. These hematologic analysis results confirm the systemic safety of the therapeutical hydrogels.

4. Conclusion

In this study, we achieved the RSM-optimized synthesis of MultiBioGel (DMH) by encapsulating MXene and DPT within the microstructures of aliphatic BH, which possessed strong and flexible properties due to its dual-crosslinked network. DMH's precursor mixture can be applied directly to wounds, with immediate sol-to-gel transition in the open air, providing shape adaptability. It demonstrated solid-like

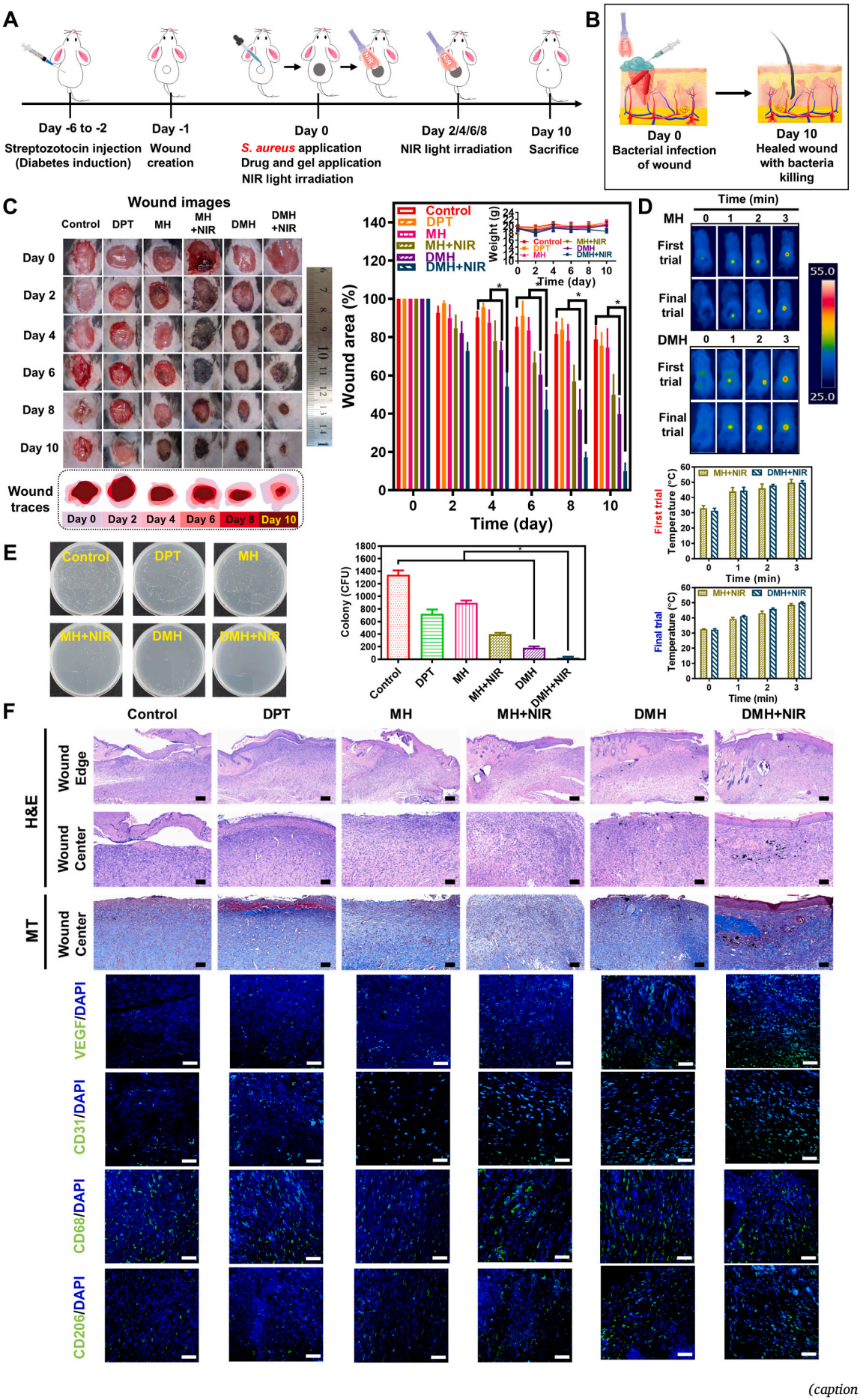

(caption on next page)

Fig. 6. *In vivo* wound healing experiment on bacteria-infected diabetic mouse models. (A) Therapy schedule illustration. (B) Illustration of bacterial wound healing. (C) Optical images of wounds, wound traces, wound healing (%), and body weight of mice (inset) on day 0 to 10 of the groups: control, DPT, MH, MH + NIR, DMH, and DMH + NIR. Each point represents mean ± SD ($n \geq 5$). *$p < 0.05$, between the indicated groups. (D) Thermal images and temperature profiles of the photothermal test. Each point represents mean ± SD ($n \geq 5$). (E) *S. aureus* bacterial colony estimation for skin tissues. Each point represents mean ± SD ($n \geq 3$). *$p < 0.05$, between the indicated groups. (F) H&E, MT, and IF (VEGF, CD31, CD68, and CD206) staining of the skins in the bacteria-infected diabetic mice on day 10. Scale bar: 100 μm.

rheological features, mechanical strength, stretchability, underwater flexibility, injectability, tissue adhesion in air/water, ROS/RNS scavenging, electrical conductivity, photothermal conversion, sustained drug release, and antibacterial activity. MXene contributed to ROS/RNS scavenging by converting toxic H_2O_2/$^{\bullet}OH$/$O_2^{\bullet-}$ and $NO^{\bullet}$/$NO_2^{\bullet}$ to non-toxic H_2O and NO_2^-/NO_3^-; antibacterial potential toward *S. aureus*/*E. coli*; and photothermal properties under NIR light. DMH showed sustained DPT release to combat gram-positive *S. aureus* infection. Cellular ROS scavenging and accelerated cell migration of DMH enhanced wound healing efficiency with an enhanced hemostatic effect. The MultiBioGel system demonstrated superior *in vivo* therapeutic efficacy in bacteria-infected and non-infected diabetic wound models, showing accelerated wound closure, enhanced skin tissue regeneration with proper organization, antibacterial activity, and improved angiogenesis. Histological analyses of vital organs and blood biochemistry confirmed the biosafety of MultiBioGel treatment, indicating potential for clinical translation in diabetic wound management. In the future, this hydrogel system could be adapted for treating other chronic wounds, post-surgical infections, or burns, especially where oxidative stress and drug-resistant infections complicate healing. Its modularity also contributes to the incorporation of other therapeutic peptides or regenerative agents, enabling personalized and multifunctional wound care platforms.

CRediT authorship contribution statement

Mrinmoy Karmakar: Writing – review & editing, Writing – original draft, Visualization, Methodology, Investigation, Formal analysis, Data curation, Conceptualization. **Sungyun Kim:** Writing – review & editing, Writing – original draft, Investigation, Formal analysis, Data curation, Conceptualization. **Han-Jun Kim:** Writing – original draft, Investigation, Formal analysis. **Ji Won Huh:** Investigation, Formal analysis. **Da In Jeong:** Investigation, Formal analysis. **Eunseo Park:** Investigation, Formal analysis. **Seongeun Kim:** Investigation, Formal analysis. **Eun-Hye Hong:** Investigation. **Jin Hyeong:** Investigation. **Dae-Joon Kim:** Investigation. **Hye Kyu Choi:** Visualization, Investigation. **Junmin Lee:** Methodology, Formal analysis, Conceptualization. **Hyun-Jeong Ko:** Resources, Methodology, Conceptualization. **Ki-Bum Lee:** Writing – original draft, Supervision, Resources, Methodology, Conceptualization. **Dae-Duk Kim:** Methodology, Conceptualization. **Hyun-Jong Cho:** Writing – review & editing, Writing – original draft, Visualization, Supervision, Resources, Project administration, Methodology, Funding acquisition, Formal analysis, Data curation, Conceptualization.

Declaration of competing interest

The authors declare that they have no known competing financial interests or personal relationships that could have appeared to influence the work reported in this paper.

Acknowledgments

This research was supported by the National Research Foundation of Korea (NRF) grant funded by the Ministry of Science and ICT and Ministry of Education (RS-2018-NR031068, 2020R1C1C1003945, and RS-2024-00352515).

Appendix A. Supplementary data

Supplementary data to this article can be found online at https://doi.org/10.1016/j.cej.2025.167327.

Data availability

Data will be made available on request.

References

[1] Z. Qian, H. Wang, Y. Bai, Y. Wang, L. Tao, Y. Wei, Y. Fan, X. Guo, H. Liu, Improving chronic diabetic wound healing through an injectable and self-healing hydrogel with platelet-rich plasma release, ACS Appl. Mater. Interfaces 12 (2020) 55659–55674.
[2] T. Wang, Y. Li, E.J. Cornel, C. Li, J. Du, Combined antioxidant–antibiotic treatment for effectively healing infected diabetic wounds based on polymer vesicles, ACS Nano 15 (2021) 9027–9038.
[3] Y. Li, R. Fu, Z. Duan, C. Zhu, D. Fan, Artificial nonenzymatic antioxidant Mxene nanosheet-anchored injectable hydrogel as a mild photothermal-controlled oxygen release platform for diabetic wound healing, ACS Nano 16 (2022) 7486–7502.
[4] B.A. Lipsky, U. Stoutenburgh, Daptomycin for treating infected diabetic foot ulcers: evidence from a randomized, controlled trial comparing daptomycin with vancomycin or semi-synthetic penicillins for complicated skin and skin-structure infections, J. Antimicrob. Chemother. 55 (2005) 240–245.
[5] P. Alka, R.R. Singh, N. Pal, N. Mishra, A. Singh, S.A. Verma, Saraf, Development of pH-sensitive hydrogel for advanced wound healing: graft copolymerization of locust bean gum with acrylamide and acrylic acid, Int. J. Pharm. 661 (2024) 124450.
[6] I.A. Duceac, L. Verestiuc, C.D. Dimitriu, V. Maier, S. Coseri, Design and preparation of new multifunctional hydrogels based on chitosan/acrylic polymers for drug delivery and wound dressing applications, Polymers 12 (2020) 1–20.
[7] H.Y. Chow, K.H.L. Po, K. Jin, G. Qiao, Z. Sun, W. Ma, X. Ye, N. Zhou, S. Chen, X. Li, Establishing the structure–activity relationship of daptomycin, ACS Med. Chem. Lett. 11 (2020) 1442–1449.
[8] G. Rizzetto, E. Molinelli, G. Radi, F. Diotallevi, O. Cirioni, L. Brescini, A. Giacometti, A. Offidani, O. Simonetti, Role of daptomycin in cutaneous wound healing: a narrative review, Antibiotics 11 (2022) 944.
[9] L. Jin, X. Guo, D. Gao, Y. Liu, J. Ni, Z. Zhang, Y. Huang, G. Xu, Z. Yang, X. Zhang, X. Jiang, An NIR photothermal-responsive hybrid hydrogel for enhanced wound healing, Bioact. Mater. 16 (2022) 162–172.
[10] H. Mondal, M. Karmakar, B. Datta, An MXene-grafted terpolymer hydrogel for adsorptive immobilization of toxic Pb(II) and post-adsorption application of metal ion hydrogel, Gels 9 (2023) 827.
[11] G. Perini, A. Rosenkranz, G. Friggeri, D. Zambrano, E. Rosa, A. Augello, V. Palmieri, M.D. Spirito, M. Papi, Advanced usage of $Ti_3C_2T_x$ MXenes for photothermal therapy on different 3D breast cancer models, Biomed. Pharmacother. 153 (2022) 113496.
[12] Y. Li, R. Fu, Z. Duan, C. Zhu, D. Fan, Artificial nonenzymatic antioxidant MXene nanosheet-anchored injectable hydrogel as a mild photothermal-controlled oxygen release platform for diabetic wound healing, ACS Nano 16 (2022) 7486–7502.
[13] A.L. Odom, New C–N and C–C bond forming reactions catalyzed by titanium complexes, Dalton Trans. (2005) (2005) 225–233.
[14] H. Park, J.-U. Kim, S. Kim, N.S. Hwang, H.D. Kim, Sprayable Ti_3C_2 MXene hydrogel for wound healing and drug release system, Mater. Today Bio 23 (2023) 100881.
[15] C. Wei, P. Tang, Y. Tang, L. Liu, X. Lu, K. Yang, Q. Wang, W. Feng, Q.T.H. Shubhra, Z. Wang, H. Zhang, Sponge-like macroporous hydrogel with antibacterial and ROS scavenging capabilities for diabetic wound regeneration, Adv. Healthc. Mater. 11 (2022) 2200717.
[16] L. Zhou, H. Zheng, Z. Liu, S. Wang, Z. Liu, F. Chen, H. Zhang, J. Kong, F. Zhou, Q. Zhang, Conductive antibacterial hemostatic multifunctional scaffolds based on $Ti_3C_2T_x$ MXene nanosheets for promoting multidrug-resistant bacteria-infected wound healing, ACS Nano 15 (2021) 2468–2480.
[17] B.S. Kaith, R. Sharma, S. Kalia, M.S. Bhatti, Response surface methodology and optimized synthesis of guar gum-based hydrogels with enhanced swelling capacity, RSC Adv. 4 (2014) 40339–40344.
[18] C.A. Schneider, W.S. Rasband, K.W. Eliceiri, NIH image to ImageJ: 25 years of image analysis, Nat. Methods 9 (2012) 671–675.
[19] M. Karmakar, H. Mondal, N.N. Ghosh, P.K. Chattopadhyay, N.R. Singha, Synthesis of gum tragacanth-grafted pentapolymer hydrogels for As(III) exclusion: roles of microwaves, RSM optimization, and DFT studies, Int. J. Biol. Macromol. 184 (2021) 909–925.

[20] X. Zhao, Y. Liang, B. Guo, Z. Yin, D. Zhu, Y. Han, Injectable dry cryogels with excellent blood-sucking expansion and blood clotting to cease hemorrhage for lethal deep-wounds, coagulopathy and tissue regeneration, Chem. Eng. J. 403 (2021) 126329.

[21] R. Haghniaz, H.J. Kim, H. Montazerian, A. Baidya, M. Tavafoghi, Y. Chen, Y. Zhu, S. Karamikamkar, A. Sheikhi, A. Khademhosseini, Tissue adhesive hemostatic microneedle arrays for rapid hemorrhage treatment, Bioact. Mater. 23 (2023) 314–327.

[22] M.U.A. Khan, S.I.A. Razaq, H. Mehboob, S. Rehman, W.S. Al-Arjan, R. Amin, Antibacterial and hemocompatible pH-responsive hydrogel for skin wound healing application: in vitro drug release, Polymers 13 (2021) 3703.

[23] Y. Danyuo, C.J. Ani, A.A. Salifu, J.D. Obayemi, S. Dozie-Nwachukwu, V. O. Obanawu, U.M. Akpan, O.S. Odusanya, M. Abade-Abugre, F. McBagonluri, W. O. Soboyejo, Anomalous release kinetics of prodigiosin from poly-N-isopropyl-acrylamid based hydrogels for the treatment of triple negative breast cancer, Sci. Rep. 9 (2019) 3862.

[24] Z. Yang, Y. Hu, P. Yue, H. Li, Y. Wu, X. Hao, F. Peng, Structure, stability, antioxidant activity, and controlled-release of selenium nanoparticles decorated with lichenan from *Usnea Longissima*, Carbohydr. Polym. 299 (2023) 120219.

[25] X. Bao, J. Zhao, J. Sun, M. Hu, X. Yang, Polydopamine nanoparticles as efficient scavengers for reactive oxygen species in periodontal disease, ACS Nano 12 (2018) 8882–8892.

[26] S. Bhubhanil, C. Talodthaisong, M. Khongkow, K. Namdee, P. Wongchitrat, W. Yingmema, J.A. Hutchison, S. Lapmanee, S. Kulchat, Enhanced wound healing properties of guar gum/curcumin-stabilized silver nanoparticle hydrogels, Sci. Rep. 11 (2021) 21836.

[27] M. Mao, J. Kong, X. Ge, Y. Sun, H. Yu, J. Liu, W. Huang, D.Y. Wang, Y. Wang, MXene-based wearable self-powered and photothermal triboelectric nanogenerator patches for wound healing acceleration and tactile sensing, Chem. Eng. J. 482 (2024) 148949.

[28] K.L. Firestein, J.E. von Treifeldt, D.G. Kvashnin, J.F.S. Fernando, C. Zhang, A. G. Kvashnin, E.V. Podryabinkin, A.V. Shapeev, D.P. Siriwardena, P.B. Sorokin, D. Golberg, Young's modulus and tensile strength of Ti_3C_2 MXene nanosheets as revealed by in situ TEM probing, AFM nanomechanical mapping, and theoretical calculations, Nano Lett. 20 (2020) 5900–5908.

[29] N.R. Singha, A. Dutta, M. Mahapatra, M. Karmakar, H. Mondal, P. K. Chattopadhyay, D.K. Maiti, Guar gum-grafted terpolymer hydrogels for ligand-selective individual and synergistic adsorption: effect of comonomer composition, ACS Omega 3 (2018) 472–494.

[30] A. Kubotera, R. Saito, Synthesis of well-defined 3-arm and 6-arm poly(acrylic acid) s via ATRP of methyl acrylate and hydrolyses of 3-arm and 6-arm poly(methyl acrylate)s, Polym. J. 48 (2016) 611–619.

[31] M. Karmakar, H. Mondal, T. Ghosh, P.K. Chattopadhyay, D.K. Maiti, N.R. Singha, Chitosan-grafted tetrapolymer using two monomers: pH-responsive high-performance removals of Cu(II), Cd(II), Pb(II), dichromate, and biphosphate and analyses of adsorbed microstructures, Environ. Res. 179 (2019) 108839.

[32] H. Mondal, M. Karmakar, P.K. Chattopadhyay, A. Halder, N.R. Singha, Scale-up one-pot synthesis of waste collagen and apple pomace pectin incorporated pentapolymer biocomposites: roles of waste collagen for elevations of properties and unary/ternary removals of Ti(IV), As(V), and V(V), J. Hazard. Mater. 409 (2021) 124873.

[33] N.R. Singha, M. Karmakar, M. Mahapatra, H. Mondal, A. Dutta, M. Deb, M. Mitra, C. Roy, P.K. Chattopadhyay, An in situ approach for the synthesis of a gum ghatti-g-interpenetrating terpolymer network hydrogel for the high-performance adsorption mechanism evaluation of Cd(II), Pb(II), Bi(III) and Sb(III), J. Mater. Chem. A 6 (2018) 8078–8100.

[34] E.G. Tótoli, H.R.N. Salgado, Fourier-transform infrared (FTIR) spectrophotometry: an ecofriendly method for the analysis of injectable daptomycin, J. AOAC Int. 100 (2017) 1569–1576.

[35] A. Müller, M. Wenzel, H. Strahl, F. Grein, T.N.V. Saaki, B. Kohl, T. Siersma, J. E. Bandow, H. Sahl, T. Schneider, L.W. Hamoen, Daptomycin inhibits cell envelope synthesis by interfering with fluid membrane microdomains, Proc. Natl. Acad. Sci. USA 113 (2016) E7077–E7086.

[36] L. Zhang, T. Ai, X. Tian, C. Xu, Y. Wu, Z. Yu, S. Dai, Microwave-assisted preparation of Ag/Fe magnetic biochar from clivia leaves for adsorbing daptomycin antibiotics, Open Chem. 20 (2022) 388–400.

[37] C. Wei, P. Tang, Y. Tang, L. Liu, X. Lu, K. Yang, Q. Wang, W. Feng, Q.T.H. Shubhra, Z. Wang, H. Zhang, Sponge-like macroporous hydrogel with antibacterial and ROS scavenging capabilities for diabetic wound regeneration, Adv. Healthc. Mater. 11 (2022) 2200717.

[38] J. Qu, X. Zhao, Y. Liang, Y. Xu, P.X. Ma, B. Guo, Degradable conductive injectable hydrogels as novel antibacterial, antioxidant wound dressings for wound healing, Chem. Eng. J. 362 (2019) 548–560.

[39] H. Zheng, S. Wang, F. Cheng, X. He, Z. Liu, W. Wang, L. Zhou, Q. Zhang, Bioactive anti-inflammatory, antibacterial, conductive multifunctional scaffold based on MXene@CeO_2 nanocomposites for infection-impaired skin multimodal therapy, Chem. Eng. J. 424 (2021) 130148.

[40] H. Zhou, L. Chen, C. Huang, Z. Jiang, H. Zhang, X. Liu, F. Zhu, Q. Wen, P. Shi, K. Liu, L. Yang, Endogenous electric field coupling MXene sponge for diabetic wound management: Haemostatic, antibacterial, and healing, J. Nanobiotechnol. 22 (2024) 530.

[41] H. Zheng, S. Wang, F. Cheng, X. He, Z. Liu, W. Wang, L. Zhou, Q. Zhang, Bioactive anti-inflammatory, antibacterial, conductive multifunctional scaffold based on MXene@CeO_2 nanocomposites for infection-impaired skin multimodal therapy, Chem. Eng. J. 424 (2021) 130148.

[42] L. Zhou, H. Zheng, Z. Liu, S. Wang, Z. Liu, F. Chen, H. Zhang, J. Kong, F. Zhou, Q. Zhang, Conductive antibacterial hemostatic multifunctional scaffolds based on $Ti_3C_2T_x$ MXene nanosheets for promoting multidrug-resistant bacteria-infected wound healing, ACS Nano 15 (2021) 2468–2480.

[43] H. Zhou, L. Chen, C. Huang, Z. Jiang, H. Zhang, X. Liu, F. Zhu, Q. Wen, P. Shi, K. Liu, L. Yang, Endogenous electric field coupling MXene sponge for diabetic wound management: Haemostatic, antibacterial, and healing, J. Nanobiotechnol. 22 (2024) 530.

[44] A. Guo, B. Song, B. Reid, Y. Gu, J.V. Forrester, C.A.B. Jahoda, M. Zhao, Effects of physiological electric fields on migration of human dermal fibroblasts, J. Invest. Dermatol. 130 (2010) 2320–2327.

[45] M. Shan, C. Gong, B. Li, G. Wu, A pH, glucose, and dopamine triple-responsive, self-healable adhesive hydrogel formed by phenylborate–catechol complexation, Polym. Chem. 8 (2017) 2997–3005.

[46] J.A. Karas, G.P. Carter, B.P. Howden, A.M. Turner, O.K.A. Paulin, J.D. Swarbrick, M.A. Baker, J. Li, T. Velkov, Structure-activity relationships of daptomycin lipopeptides, J. Med. Chem. 63 (2020) 13266–13290.

[47] S.D. Taylor, M. Palmer, The action mechanism of daptomycin, Bioorg. Med. Chem. 24 (2016) 6253–6268.

[48] M. Heidary, A.D. Khosravi, S. Khoshnood, M.J. Nasiri, S. Soleimani, M. Goudarzi, Daptomycin, J. Antimicrob. Chemother. 73 (2018) 1–11.

[49] C. Ardean, C.M. Davidescu, N.S. Nemeş, A. Negrea, M. Ciopec, N. Duteanu, P. Negrea, D. Duda-seiman, V. Musta, Factors influencing the antibacterial activity of chitosan and chitosan modified by functionalization, Int. J. Mol. Sci. 22 (2021) 7449.

[50] K. Rasool, M. Helal, A. Ali, C.E. Ren, Y. Gogotsi, K.A. Mahmoud, Antibacterial activity of $Ti_3C_2T_x$ MXene, ACS Nano 10 (2016) 3674–3684.

[51] M.S. Khan, H.N. Abdelhamid, H.F. Wu, Near infrared (NIR) laser mediated surface activation of graphene oxide nanoflakes for efficient antibacterial, antifungal and wound healing treatment, Colloids Surf. B: Biointerfaces 127 (2015) 281–291.

[52] C.P. Randall, K.R. Mariner, I. Chopra, A.J. O'Neill, The target of daptomycin is absent from Escherichia coli and other gram-negative pathogens, Antimicrob. Agents Chemother. 57 (2013) 637–639.

[53] X. Lai, Y. Tang, Y. Dong, Y. Luo, X. Yang, Q. Peng, Multifunctional MXene nanosheets and their applications in antibacterial therapy, Adv. NanoBiomed Res. 4 (2024) 2400033.

[54] C. Ding, Z. Guo, J. Xiong, D. Wu, Y. Tao, Y. Qin, Y. Kong, Rational design of a multi-responsive drug delivery platform based on SiO_2 @PPy@poly(acrylic acid-co-acrylamide), React. Funct. Polym. 137 (2019) 88–95.

[55] Y. Li, C. Xiong, H. Huang, X. Peng, D. Mei, M. Li, G. Liu, M. Wu, T. Zhao, B. Huang, 2D $Ti_3C_2T_x$ MXenes: visible black but infrared white materials, Adv. Mater. 33 (2021) 2103054.

[56] H. Shin, W. Jeong, T.H. Han, Maximizing light-to-heat conversion of $Ti_3C_2T_x$ MXene metamaterials with wrinkled surfaces for artificial actuators, Nat. Commun. 15 (2024) 10507.

[57] X. Zhang, G. Cheng, X. Xing, J. Liu, Y. Cheng, T. Ye, Q. Wang, X. Xiao, Z. Li, H. Deng, Near-infrared light-triggered porous AuPd alloy nanoparticles to produce mild localized heat to accelerate bone regeneration, J. Phys. Chem. Lett. 10 (2019) 4185–4191.

[58] X. Zhang, B. Tan, Y. Wu, M. Zhang, J. Liao, A review on hydrogels with photothermal effect in wound healing and bone tissue engineering, Polymers 13 (2021) 2100.

[59] D.I. Jeong, H.J. Kim, S.Y. Lee, S. Kim, J.W. Huh, J.H. Ahn, M. Karmakar, H.J. Kim, K.J. Lee, J. Lee, H.J. Ko, H.J. Cho, Hydrogel design to overcome thermal resistance and ROS detoxification in photothermal and photodynamic therapy of cancer, J. Control. Release 366 (2024) 142–159.

[60] X. Qi, Y. Huang, S. You, Y. Xiang, E. Cai, R. Mao, W. Pan, X. Tong, W. Dong, F. Ye, J. Shen, Engineering robust Ag-decorated polydopamine nano-photothermal platforms to combat bacterial infection and prompt wound healing, Adv. Sci. 9 (2022) 2106015.

[61] C. Chen, P. Zhou, C. Huang, R. Zeng, L. Yang, L. Han, Y. Qu, C. Zhang, Photothermal-promoted multi-functional dual network polysaccharide hydrogel adhesive for infected and susceptible wound healing, Carbohydr. Polym. 273 (2021) 118557.

[62] P. Sim, X.L. Strudwick, Y.M. Song, A.J. Cowin, S. Garg, Influence of acidic pH on wound healing in vivo: a novel perspective for wound treatment, Int. J. Mol. Sci. 23 (2022) 13655.

[63] W. Zhu, J. Long, M. Shi, Release kinetics model fitting of drugs with different structures from viscose fabric, Materials 16 (2023) 3282.

[64] J. Liu, W. Lu, X. Lu, L. Zhang, H. Dong, Y. Li, Versatile $Ti_3C_2T_x$ MXene for free-radical scavenging, Nano Res. 15 (2022) 2558–2566.

[65] H. Geng, Y. Ren, G. Qin, T. Wen, Q. Liu, H. Xu, W. He, Ti_3C_2 nanosheets with broad-spectrum antioxidant activity for cytoprotection against oxidative stress, RSC Adv. 12 (2022) 11128–11138.

[66] D.P. Sahu, S.N. Jammalamadaka, Detection of bovine serum albumin using hybrid TiO_2 + graphene oxide based bio–resistive random access memory device, Sci. Rep. 9 (2019) 16141.

[67] R.A. Soomro, P. Zhang, B. Fan, Y. Wei, B. Xu, Progression in the oxidation stability of MXenes, Nano Micro Lett. 15 (2023) 108.

[68] H. Kim, X. Xue, Detection of total reactive oxygen species in adherent cells by 2′,7′-dichlorodihydrofluorescein diacetate staining, J. Vis. Exp. 160 (2020), https://doi.org/10.3791/60682.

[69] D. Zhang, Q. Chen, Y. Bi, H. Zhang, M. Chen, J. Wan, C. Shi, W. Zhang, J. Zhang, Z. Qiao, J. Li, S. Chen, R. Liu, Bio-inspired poly-DL-serine materials resist the foreign-body response, Nat. Commun. 12 (2021) 5327.

[70] X. Liu, L. Gao, S. Fu, W. Zhao, F. Wang, J. Gao, C. Li, H. Wu, L. Wang, Polycaprolactone nanofiber-alginate hydrogel interpenetrated skin substitute for regulation of wound-substitute interface, Mater. Des. 227 (2023) 111706.
[71] C. Lin, T.W. Lu, F.Y. Hsu, T.W. Huang, M.H. Ho, H.T. Lu, F.L. Mi, An injectable *in situ*-forming hydrogel with self-activating genipin-chitosan (GpCS) cross-linking and an O_2/Ca^{2+} self-supplying capability for wound healing and rapid hemostasis, Carbohydr. Polym. 351 (2025) 123051.
[72] Y. Chen, J. Cai, D. Liu, S. Liu, D. Lei, L. Zheng, Q. Wei, M. Gao, Zinc-based metal organic framework with antibacterial and anti-inflammatory properties for promoting wound healing, Regen. Biomater. 9 (2022) 19.
[73] D. Luo, H.Q. Zhang, X.Y. Xuanyuan, D. Deng, Z.M. Lu, W.S. Liu, M. Li, MXene-derived multifunctional biomaterials: new opportunities for wound healing, Biomater. Res. 29 (2025) 0143.
[74] M. Liu, L. Zheng, K. Zha, Y. Yang, Y. Hu, K. Chen, F. Wang, K. Zhang, W. Liu, B. Mi, X. Xiao, Q. Feng, Cu(II)@MXene based photothermal hydrogel with antioxidative and antibacterial properties for the infected wounds, Front. Bioeng. Biotechnol. 9 (2023) 1308184.
[75] M. Heidary, A.D. Khosravi, S. Khoshnood, M.J. Nasiri, S. Soleimani, M. Goudarzi, Daptomycin, J. Antimicrob. Chemother. 73 (2018) 1–11.
[76] S. Guo, Y. Ren, R. Chang, Y. He, D. Zhang, F. Guan, M. Yao, Injectable self-healing adhesive chitosan hydrogel with antioxidative, antibacterial, and hemostatic activities for rapid hemostasis and skin wound healing, ACS Appl. Mater. Interfaces 14 (2022) 34455–34469.
[77] A. Shamloo, Z. Aghababaie, H. Afjoul, M. Jami, M.R. Bidgoli, M. Vossoughi, A. Ramazani, K. Kamyabhesari, Fabrication and evaluation of chitosan/gelatin/PVA hydrogel incorporating honey for wound healing applications: an in vitro, in vivo study, Int. J. Pharm. 592 (2021) 120068.
[78] V. Castrejón-Comas, N. Mataró, L. Resina, D. Zanuy, Q. Nuñez-Aulina, J. Sánchez-Morán, H. Enshaei, M. Arnau, H. Muñoz-Galán, J.C. Worch, A.P. Dove, C. Alemán, M.M. Pérez-Madrigal, Electro-responsive hyaluronic acid-based click-hydrogels for wound healing, Carbohydr. Polym. 348 (2025) 122941.
[79] C. Shi, Y. Zhang, G. Wu, Z. Zhu, H. Zheng, X. Sun, Y. Heng, S. Pan, H. Xiu, J. Zhang, Z. Yin, Z. Yu, B. Liang, Hyaluronic acid-based reactive oxygen species-responsive multifunctional injectable hydrogel platform accelerating diabetic wound healing, Adv. Healthc. Mater. 13 (2024) 2302626.